

CORRIGENDUM

JASON E. SMERDON AND ALEXEY KAPLAN

Lamont-Doherty Earth Observatory, Columbia University, Palisades, New York

DIANA CHANG

Tri-Institutional Training Program in Computational Biology and Medicine, Cornell University, Ithaca, New York

MICHAEL N. EVANS

Department of Geology and Earth Systems Science Interdisciplinary Center, University of Maryland, College Park, College Park, Maryland

(Manuscript received 5 October 2010, in final form 6 October 2010)

Due to a production error, Smerdon et al. (2010) was mistakenly published without the final corrections implemented in the text. To correct this, the following pages contain the full article as it should have appeared, with the final edits included.

The staff of the *Journal of Climate* regrets any inconvenience this error may have caused.

REFERENCE

Smerdon, J. E., A. Kaplan, D. Chang, and M. N. Evans, 2010: A pseudoproxy evaluation of the CCA and RegEM methods for reconstructing climate fields of the last millennium. *J. Climate*, **23**, 4856–4880.

A Pseudoproxy Evaluation of the CCA and RegEM Methods for Reconstructing Climate Fields of the Last Millennium*

JASON E. SMERDON AND ALEXEY KAPLAN

Lamont-Doherty Earth Observatory, Columbia University, Palisades, New York

DIANA CHANG

Tri-Institutional Training Program in Computational Biology and Medicine, Cornell University, Ithaca, New York

MICHAEL N. EVANS

Department of Geology and Earth Systems Science Interdisciplinary Center, University of Maryland, College Park, College Park, Maryland

(Manuscript received 1 July 2009, in final form 29 April 2010)

ABSTRACT

Canonical correlation analysis (CCA) is evaluated for paleoclimate field reconstructions in the context of pseudoproxy experiments assembled from the millennial integration (850–1999 C.E.) of the National Center for Atmospheric Research Community Climate System Model, version 1.4. A parsimonious method for selecting the order of the CCA model is presented. Results suggest that the method is capable of resolving multiple (3–13) climatic patterns given the estimated proxy observational network and the amount of observational uncertainty. CCA reconstructions are compared to those derived from the regularized expectation maximization method using ridge regression regularization (RegEM-Ridge). CCA and RegEM-Ridge yield similar skill patterns that are characterized by high correlation regions collocated with dense pseudoproxy sampling areas in North America and Europe. Both methods also produce reconstructions characterized by spatially variable warm biases and variance losses, particularly at high pseudoproxy noise levels. RegEM-Ridge in particular is subject to significantly larger variance losses than CCA, even though the spatial correlation patterns of the two methods are comparable. Results collectively indicate the importance of evaluating the field performance of methods that target spatial climate patterns during the last several millennia and indicate that the results of currently available climate field reconstructions should be interpreted carefully.

1. Introduction

A concerted research effort over the last decade has focused on reconstructing global or hemispheric climate during the last millennium using networks of climate proxies (e.g., Folland et al. 2001; Jansen et al. 2007; North et al. 2006; Jones and Mann 2004; Jones et al. 2009). These efforts are in many ways an outgrowth of earlier studies that developed reconstructions on regional scales,

particularly pioneering work in dendroclimatology that extends back to the 1960s and 1970s (e.g., Fritts et al. 1971). Recent efforts have employed single-proxy (e.g., Cook et al. 1994, 2004; Briffa 2000; Briffa et al. 2001; Esper et al. 2002; Evans et al. 2002; D'Arrigo et al. 2006, 2009) or multiproxy statistical approaches (Mann et al. 1998, 1999, 2005, 2007a, 2008; Jones et al. 1998; Crowley and Lowery 2000; Rutherford et al. 2005; Moberg et al. 2005; Hegerl et al. 2007) to calibrate proxy records on observational data during their period of overlap and subsequently to reconstruct past climate variability using derived climate-proxy relationships. Various efforts have demonstrated the promise of these approaches (Cook et al. 1994, 2004; Mann et al. 1998, 1999; Evans et al. 2002; Luterbacher et al. 1999; Rutherford et al. 2005; Casty et al. 2005; Pauling et al. 2006; Hegerl et al. 2007), but in some cases results and methodologies have been vigorously debated

* Lamont-Doherty Earth Observatory Contribution Number 7377.

Corresponding author address: Jason E. Smerdon, Lamont-Doherty Earth Observatory, Columbia University, 61 Route 9W, P.O. Box 1000, Palisades, NY 10964.
E-mail: jsmerdon@ldeo.columbia.edu

(Broecker 2001; Huang et al. 2000; Harris and Chapman 2001; Esper et al. 2002; Beltrami 2002; González-Rouco et al. 2003, 2006; von Storch et al. 2004, 2006; Pollack and Smerdon 2004; Rutherford and Mann 2004; McIntyre and McKittrick 2005; Xoplaki et al. 2005; von Storch and Zorita 2005; Bürger and Cubasch 2005; Huybers 2005; Wahl et al. 2006; Bürger et al. 2006; Zorita et al. 2007; Lee et al. 2007; Smerdon and Kaplan 2007; Smerdon et al. 2008b; Wahl and Ammann 2007; Ammann and Wahl 2007; Mann et al. 2003, 2005, 2007a,b,c, 2008, 2009; Moberg et al. 2005, 2008; Hegerl et al. 2007; Küttel et al. 2007; Christiansen et al. 2009). One of the principal issues of this debate surrounds the magnitude of reconstructed temperature variability during the last millennium on decadal and longer time scales, particularly as it relates to the magnitude, phasing, and ubiquity of the putative Medieval Climatic Anomaly and Little Ice Age (e.g., Hughes and Diaz 1994; Broecker 2001; Mann 2002; Bradley et al. 2003; Mann et al. 2003, 2005, 2007a,b,c, 2009). Although a great deal of progress has been made to understand how various reconstructions may accurately represent the characteristics of these past epochs, there remain important unanswered questions about reconstruction uncertainties. These questions are tied to understanding, for example, the impact of proxy distributions and abundance, the connections between climate and proxy responses across different spectral domains, the response of proxies to multiple environmental variables, and the role of teleconnections and noise in the calibration data—questions that are ultimately fundamental to the success of efforts to reconstruct past climatic variability (e.g., North et al. 2006; Jansen et al. 2007).

An additional element of uncertainty in climate reconstructions that has recently gained more attention is the degree to which specific reconstruction methodologies impose their own error and biases on derived reconstructions. Here we focus specifically on the uncertainties in hemispheric-scale temperature reconstructions of the past millennium that arise principally from the applied methodology. Reconstruction methods for this purpose generally can be divided into two groups: one in which individual indices are targeted (see discussion in Mann et al. 2005) and climate field reconstruction (CFR) methods (Evans et al. 2001). Index methods target mean hemispheric or global temperature time series as a predictand, therefore yielding reconstructions of only these individual indices (e.g., Groveman and Landsberg 1979; Esper et al. 2002, 2005; Crowley and Lowery 2000; Moberg et al. 2005; Hegerl et al. 2007; D'Arrigo et al. 2006; Mann et al. 2007a, 2008). Although index methods have the disadvantage of offering no spatial information, they have the benefit of being more straightforward, robust, and likely require no more than a few tens of predictors for skillful

reconstructions of hemispheric or global temperature variability (e.g., Crowley and Lowery 2000; Hegerl et al. 2007). In contrast to index approaches, CFR methods attempt to reconstruct spatial patterns of temperature variability, which is the fundamental promise of these methods (e.g., Cook et al. 1994; Mann et al. 1998, 1999, 2005, 2007a, 2009; Rutherford et al. 2005; Evans et al. 2002; Luterbacher et al. 2004; Xoplaki et al. 2005). CFR methods can be complicated, however, by the ill-conditioned nature of the problem, are more dependent on the stability of climate-proxy connections and climate teleconnections, and require more extensive distributions of proxies than index reconstructions.

In spite of the differences between index and CFR methods, the debate surrounding temperature reconstructions of the last millennium has almost exclusively been limited to comparisons between mean Northern Hemisphere (NH) or global time series (e.g., Briffa and Osborn 2002; Jones and Mann 2004; North et al. 2006; Folland et al. 2001; Jansen et al. 2007); in the case of CFRs, these mean time series are computed from the underlying reconstructed fields. Consequently, there have been few assessments of the robustness of spatial patterns in the collection of available CFRs. Some field comparisons of CFRs have been done on regional scales. Cook et al. (1994) compared two CFR techniques applied to dendroclimatic series in western Europe and eastern North America and found them to produce similar results. Similarly, Zhang et al. (2004) investigated two methods for drought reconstructions over the continental United States and also found their performance comparable. A more recent study has compared the field skill of two temperature field reconstruction methods over the North Atlantic and the European continent (Riedwyl et al. 2009). At global and hemispheric scales, however, proxy distributions are more diffuse, predictor networks comprise multiple proxies, and teleconnection patterns are likely more essential to the skill of the reconstruction. It therefore is crucial to evaluate not only the mean global or hemispheric characteristics of CFRs but also the spatial skill of the fields derived from these methods.

A significant challenge for CFR comparisons is that researchers must use proxy networks of opportunity and thus of variable composition in proxy type, location, and temporal extent. Uncertainty in any given reconstruction is therefore the combination of uncertainties in the method used, the spatial sampling of the proxy network, and the actual climate-proxy connection of each of the proxy series used in the network. If the objective is to isolate the impact of one of these factors, it is difficult to do so from comparisons between these real-world CFR results. The advent of pseudoproxy experiments (Mann and Rutherford 2002) has circumvented some of these

challenges, however, by granting a consistent test bed on which to test reconstruction methodologies (González-Rouco et al. 2006; von Storch et al. 2004, 2006; Mann et al. 2005, 2007a; Hegerl et al. 2007; Smerdon and Kaplan 2007; Smerdon et al. 2008b; Lee et al. 2007; Küttel et al. 2007; Riedwyl et al. 2009; Christiansen et al. 2009; Tingley and Huybers 2010a,b).

Pseudoproxy experiments have typically employed millennial integrations from general circulation models (GCMs) that only recently have become available (González-Rouco et al. 2003, 2006; Ammann et al. 2007). These experiments are generally performed with the following steps: 1) the complete GCM field is subsampled to mimic the availability of instrumental and proxy information in real-world climate reconstructions of the last millennium; 2) the time series that represent proxy information are perturbed to simulate the spatial and temporal noise characteristics present in real-world proxies; 3) reconstruction algorithms are applied to the model-sampled pseudo “instrumental data” and pseudoproxy series to derive a reconstruction of the climate simulated by the GCM; and 4) the derived reconstruction is compared to the known model target. There are, indeed, some open questions associated with these experiments, such as whether the adopted noise models in the pseudoproxy network are realistic and how well the model statistics represent real-world climate characteristics that affect reconstruction skill (e.g., teleconnections). Nevertheless, the utility of pseudoproxy experiments lies in their ability to provide an objective dataset on which to test reconstruction methods. While future improvements in the implementation of pseudoproxy tests will undoubtedly be made, much insight into the performance of multiple reconstruction methods has already been gained from this approach (von Storch et al. 2004, 2006; Mann et al. 2005, 2007a; Smerdon and Kaplan 2007; Lee et al. 2007; Küttel et al. 2007; Hegerl et al. 2007; Riedwyl et al. 2009; Moberg et al. 2008; Smerdon et al. 2008b; Christiansen et al. 2009; Tingley and Huybers 2010a,b).

Here we investigate skill and uncertainty in CFRs arising from the application of a reconstruction algorithm using canonical correlation analysis (CCA). CCA is a well-established method within the climate sciences (e.g., Anderson 1984; Barnett and Preisendorfer 1987; Bretherton et al. 1992; Cook et al. 1994; Wilks 1995; von Storch and Zwiers 1999; Luterbacher et al. 2000; Tippett et al. 2003, 2008), but it has not been widely applied for the purpose of deriving large-scale temperature CFRs. [CCA is mentioned briefly in Mann et al. (1998) as being unsuitable for their purposes and has more recently been applied by Christiansen et al. (2009) as one of a number of methods tested in the context of reconstructed NH means.] Our purposes herein are to evaluate in detail the

application of CCA for reconstructing NH temperatures during the last millennium and to specifically focus on the field characteristics of the derived CFRs.

In addition to investigating the performance of CCA, we compare CCA-derived results to those obtained using the regularized expectation maximization (RegEM) method (Schneider 2001). RegEM is a recently favored method for temperature reconstructions (e.g., Rutherford et al. 2005; Mann et al. 2005, 2007a, 2008, 2009), but pseudoproxy experiments also have shown some implementations of RegEM to be susceptible to warm biases and variance losses (Smerdon and Kaplan 2007; Smerdon et al. 2008b; Riedwyl et al. 2009; Christiansen et al. 2009). These findings are consistent with previous pseudoproxy experiments that have demonstrated similar behavior associated with the Mann et al. (1998, 1999) CFR method (von Storch et al. 2004, 2006). Because the application of CCA requires selection of only three model dimensions, it is straightforward to assess the skill of the method and computationally cheap to construct all possible models. This latter characteristic is in contrast to the iterative and more computationally expensive RegEM algorithm. Hence, comparison of the two methods can help elucidate the strengths and weaknesses of each.

2. Data

We use pseudoproxies derived from the millennial simulation (850–1999 C.E.) of the National Center for Atmospheric Research (NCAR) Community Climate System Model (CCSM), version 1.4, a coupled atmosphere–ocean GCM that has been driven with natural and anthropogenic forcings (Ammann et al. 2007). The simulated model field of annual surface temperature means has been interpolated to a 5° longitude–latitude grid using bilinear interpolation (Smerdon et al. 2008a; Rutherford et al. 2008). Multiple previous studies have used this field with an incorrect geographic orientation and thus sampled pseudoproxies from unintended locations (Smerdon et al. 2010). Here we use the correct field orientation and the intended pseudoproxy locations as represented in Fig. 1. These 104 pseudoproxies were sampled from the 5° gridbox locations that approximate the actual proxy locations of the Mann et al. (1998) multiproxy network. White noise at four different levels was added to model temperature time series from these selected locations to produce pseudoproxy time series with signal-to-noise ratios (SNRs), by standard deviation, of infinity (noise free), 1.0, 0.5, and 0.25.

We also used a subsampling of the CCSM mean annual temperature field to approximate the availability of instrumental temperature data. Grid points missing more than 30% of the annual data between 1856 and

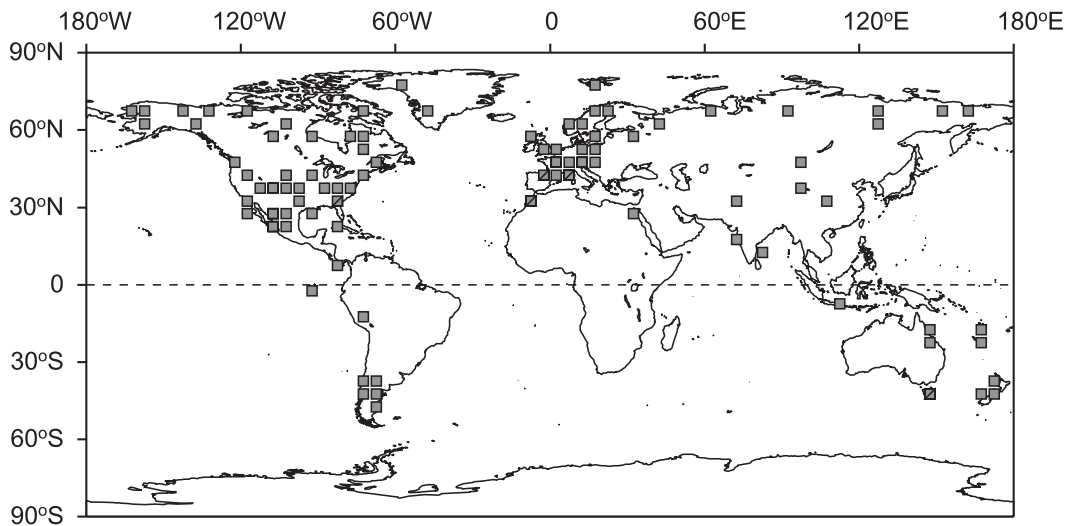


FIG. 1. Map of gridcell locations for the pseudoproxy network chosen to approximate the Mann et al. (1998) proxy locations.

1998 C.E. in the Jones et al. (1999) dataset were excluded from use as target data as described by Mann and Rutherford (2002). This restriction limits the total number of grid cells to 669 in the 0° – 70° N region (the target region). Also in keeping with instrumental data restrictions, the subsampled instrumental (calibration) data are constrained to 1856–1980 C.E.—all the annual temperature values within this period are retained for each targeted temperature grid. Note that the aforementioned error regarding the incorrect geographic orientation of the CCSM temperature field also affected the applied instrumental data mask in previous studies (Smerdon et al. 2010); our experiments herein have applied the correct mask as intended by these earlier studies.

3. Methods

a. Least squares CFRs as multivariate linear regression

Multivariate linear regression is the underlying formalism of most CFR methods used to date. The fundamental approach relates a matrix of climate proxies to a matrix of climate data during a common time interval (generally termed the calibration interval) using a linear model. For instance, let \mathbf{P} be an $m \times n$ matrix of proxy values and \mathbf{T} be an $r \times n$ matrix of instrumental temperature records, where m is the number of proxies, r is the number of spatial locations in the instrumental field, and n is the temporal dimension corresponding to the period of overlap between the proxy and instrumental data. We write the regression of \mathbf{T} columns on \mathbf{P} columns

for time-standardized matrices (\mathbf{T}' and \mathbf{P}') with rows that have means of zero and standard deviations of one:

$$\mathbf{T} = \mathbf{M}_t + \mathbf{S}_t \mathbf{T}', \quad \mathbf{P} = \mathbf{M}_p + \mathbf{S}_p \mathbf{P}',$$

where \mathbf{M}_t is a matrix of identical columns obtained by averaging \mathbf{T} in its row direction, and \mathbf{S}_t is a diagonal matrix with elements that are the standard deviations of the rows of matrix \mathbf{T} ; \mathbf{M}_p and \mathbf{S}_p are similarly defined for matrix \mathbf{P} . In these terms,

$$\mathbf{T}' = \mathbf{B} \mathbf{P}' + \varepsilon, \quad (1)$$

where \mathbf{B} is a matrix of regression coefficients with dimensions $r \times m$, and ε is the residual error. The error variances of all the elements of ε in (1) are simultaneously minimized if \mathbf{B} is chosen as

$$\mathbf{B} = (\mathbf{T}' \mathbf{P}'^T) (\mathbf{P}' \mathbf{P}'^T)^{-1}, \quad (2)$$

where the superscript T denotes the matrix transpose. Temperature thus can be predicted, or “reconstructed,” using this regression matrix during periods in which proxy data are available:

$$\hat{\mathbf{T}} = \mathbf{M}_t + \mathbf{S}_t \mathbf{B} \mathbf{S}_p^{-1} (\mathbf{P} - \mathbf{M}_p), \quad (3)$$

where $\hat{\mathbf{T}}$ denotes a matrix of reconstructed temperature values.

While the above formalism is straightforward, it works best when the system is overdetermined; that is, the time dimension n is much larger than the spatial dimension m

because the covariances are more reliably estimated. The challenge for CFR methods involves the manner in which \mathbf{B} is estimated in practical situations when this condition is not met. It is often the case in climate applications that the number of target variables exceeds the time dimension, yielding a rank-deficient problem. For instance, in most global or NH CFRs, the number of grid cells in the climate field is typically on the order of many hundreds or a few thousands, while the observational record usually contains 150 annual fields or less. The number of proxies is typically on the order of a few tens to hundreds, which may exceed or at least be comparable to the time dimension. In such cases, the cross-covariance matrix $\langle \mathbf{T}'\mathbf{P}'^T \rangle$ and covariance matrix $\langle \mathbf{P}'\mathbf{P}'^T \rangle$ cannot be well estimated. The inversion in (2) therefore requires some form of regularization. Published linear methods for global temperature CFRs vary primarily in the form of this regularization. In the following sections, we discuss CCA and RegEM as the two regularization approaches considered in this manuscript.

b. Canonical correlation analysis

For the purposes described herein, we outline the Barnett and Preisendorfer (1987) version of CCA formalism as presented by Tippett et al. (2003, 2008). This formalism as applied to the CFR problem is presented in detail in the appendix and summarized below. Two elements of the CCA application involve the eigenvalue decomposition and subsequent truncation of the proxy and temperature matrices. Both of these reductions are helpful in real-world applications where the temperature and proxy fields each contain noise or small scale features that cannot be reliably calibrated. Retaining a subset of empirical orthogonal functions in both fields can therefore guard against the possibility of calibrating modes dominated by noise or local variability. CCA in particular can be susceptible to random sampling fluctuations when the number of temporal observations is significantly less than the number of spatial locations in the target field (e.g., Barnett and Preisendorfer 1987; Bretherton et al. 1992), as is the case in the present CFR context. Over short time intervals, these random fluctuations can cause artificially high correlations between patterns that account for very little variance in either field, causing instabilities in the solutions due to sampling variability. Prefiltering the proxy and temperature matrices by retaining only a few leading modes therefore can improve the stability of CCA solutions. With regard to the reduction of the temperature field specifically, there are examples in the literature of CFR approaches that choose to either neglect or adopt a reduction of the field (e.g., Luterbacher et al. 2004; Mann

et al. 2007a). Although we build the potential for reduction of the temperature field into the CCA formalism, the degree of reduction is determined from a cross-validation scheme that does not a priori require truncation. This scheme is discussed later in the manuscript and provides an objective means of determining whether reduction is warranted and by how much.

Decomposition of the standardized proxy matrix \mathbf{P}' during the calibration interval using singular value decomposition (SVD) (Golub and Van Loan 1996) is written as

$$\mathbf{P}' = \mathbf{U}_p \mathbf{\Sigma}_p \mathbf{V}_p^T, \quad (4)$$

where the columns of \mathbf{U}_p represent spatial patterns (EOFs) and the principal components (PCs) $\mathbf{\Sigma}_p \mathbf{V}_p$ are mutually orthogonal time series that combine with the EOF patterns to produce the original dataset. The diagonal matrix $\mathbf{\Sigma}_p$ contains the nonnegative singular values, with squares proportional to the variance captured by the corresponding EOF–PC pairs. If the diagonal elements of $\mathbf{\Sigma}_p$ decrease quickly, as is often the case in climatological data where leading climate patterns dominate over many more weakly expressed local patterns or noise, a reduced-rank representation of \mathbf{P}' using only a few leading EOF–PC pairs is a good approximation of the full-rank version. Thus, we employ a reduced-rank representation of \mathbf{P}' such that d_p EOF–PC pairs are retained,

$$\mathbf{P}^r = \mathbf{U}'_p \mathbf{\Sigma}'_p \mathbf{V}'_p{}^T. \quad (5)$$

Here \mathbf{P}^r denotes the reduced-rank representation of \mathbf{P}' , and matrices with the superscript r are the truncated versions of the SVD factors corresponding to the retained number of d_p singular values. Similarly, the reduced-rank version of \mathbf{T}' is written as

$$\mathbf{T}^r = \mathbf{U}'_t \mathbf{\Sigma}'_t \mathbf{V}'_t{}^T, \quad (6)$$

where \mathbf{T}^r only uses d_t singular values and the corresponding number of singular vectors. Note that $\text{rank}(\mathbf{P}^r) = d_p$ and $\text{rank}(\mathbf{T}^r) = d_t$, whereas $\text{rank}(\mathbf{P}') = \min(m, n - 1)$ and $\text{rank}(\mathbf{T}') = \min(r, n - 1)$, in the general case.

The above decompositions can be substituted into (2), and the corresponding matrix of regression coefficients written as

$$\begin{aligned} \mathbf{B}_{\text{cca}} &= \mathbf{U}'_t \mathbf{\Sigma}'_t \mathbf{V}'_t{}^T \mathbf{V}'_p (\mathbf{\Sigma}'_p)^{-1} \mathbf{U}'_p{}^T \\ &= \mathbf{U}'_t \mathbf{\Sigma}'_t \mathbf{O}'_t \mathbf{\Sigma}'_{\text{cca}} \mathbf{O}'_p{}^T (\mathbf{\Sigma}'_p)^{-1} \mathbf{U}'_p{}^T, \end{aligned}$$

where $\mathbf{O}'_t \mathbf{\Sigma}'_{\text{cca}} \mathbf{O}'_p{}^T$ is the truncated SVD of the cross-covariance matrix $\mathbf{V}'_t{}^T \mathbf{V}'_p$ in which d_{cca} leading canonical

coefficients have been retained. From the formal derivation in the appendix, the above expression for \mathbf{B}_{cca} takes a simple form:

$$\mathbf{B}_{\text{cca}} = \mathbf{C}_t \boldsymbol{\Sigma}_{\text{cca}}^r \mathbf{W}_p^T, \quad (7)$$

where $\mathbf{C}_t = \mathbf{U}_t^r \boldsymbol{\Sigma}_t^r \mathbf{O}_t^r$ has the CCA temperature patterns in its columns, and $\mathbf{W}_p = \mathbf{U}_p^r (\boldsymbol{\Sigma}_p^r)^{-1} \mathbf{O}_p^r$ is the CCA proxy weighting matrix.

Applying \mathbf{B}_{cca} to \mathbf{P}' so as to reconstruct \mathbf{T}' is therefore equivalent to a three-step procedure:

- (i) use the weighting patterns \mathbf{W}_p to convert \mathbf{P}' into the CCA time series,

$$\mathbf{Q}_p^T = \mathbf{W}_p^T \mathbf{P}';$$

- (ii) scale these time series by the canonical correlations, that is, the diagonal elements of $\boldsymbol{\Sigma}_{\text{cca}}^r$, to produce the CCA time series for temperature,

$$\hat{\mathbf{Q}}_t^T = \boldsymbol{\Sigma}_{\text{cca}}^r \hat{\mathbf{Q}}_p^T,$$

- (iii) use the \mathbf{C}_t patterns to reconstruct a standardized version of the temperature fields,

$$\hat{\mathbf{T}}' = \mathbf{C}_t \hat{\mathbf{Q}}_t^T.$$

Note that in our formulated pseudoproxy experiments the actual CCA temperature time series,

$$\mathbf{Q}_t^T = \mathbf{W}_t^T \mathbf{T}',$$

during the reconstruction period can be directly compared with their prediction on the basis of the proxies in item (ii) above. The use of these statistics is illustrated further in section 4b(1).

For the nonstandardized version of temperature fields and proxies given in (3), the CCA temperature CFR becomes

$$\hat{\mathbf{T}} = \mathbf{M}_t + \mathbf{S}_t \mathbf{B}_{\text{cca}} \mathbf{S}_p^{-1} (\mathbf{P} - \mathbf{M}_p). \quad (8)$$

Performing this reconstruction thus requires the determination of five matrices: two in which all columns contain the mean vectors for the temperature field and the proxies, \mathbf{M}_t and \mathbf{M}_p ; the two diagonal matrices of the temperature and proxy standard deviations, \mathbf{S}_t and \mathbf{S}_p ; and the CCA low-rank regression matrix \mathbf{B}_{cca} . Under the assumption of stationarity between the mutual proxy and climate statistics, (8) can be used to reconstruct temperatures in any temporal interval, including those outside of the calibration period. The only formal

change is in the number of columns in matrices \mathbf{M}_t and \mathbf{M}_p , which of course change to match the length of the given reconstruction period.

The operator \mathbf{B}_{cca} is a reduced-rank ($\text{rank}(\mathbf{B}_{\text{cca}}) = d_{\text{cca}}$) representation of the standard multivariate regression operator. Given calibration interval datasets \mathbf{T} and \mathbf{P} , the matrix \mathbf{B}_{cca} is completely determined upon the selection of three parameters for truncated ranks, d_{cca} , d_p , and d_t . Note that traditional applications of CCA did not involve rank reductions of the predictor and predictand matrices and thus only depended on d_{cca} (see the discussion in Bretherton et al. 1992). Steps for reducing these matrix ranks by selecting d_p and d_t parameters prior to estimating the CCA time series and maps were added by Barnett and Preisendorfer (1987)—termed the BP method by Bretherton et al. (1992). Tippett et al. (2003) and Christiansen et al. (2009) used and referred to this latter BP version as CCA, as we do in this study. For some special subsets of dimensional selections, the CCA formalism reduces to other specialized forms of multivariate regression. For instance, CCA reduces to PC regression if the target field rank is not reduced and $d_{\text{cca}} = \min(d_p, d_t)$. PC regression has been applied in multiple paleoclimate contexts (e.g., Luterbacher et al. 2004), and further research on the relative performance of CCA and PC regression is warranted. Cogent discussions about the connection between CCA and multiple multivariate regression methods can be found in Barnett and Preisendorfer (1987), Bretherton et al. (1992), Cherry (1996), von Storch and Zwiers (1999), and Tippett et al. (2008).

c. CCA model–dimension selection

Appropriate selections of the d_{cca} , d_p , and d_t dimensions are crucial for the application of the CCA method. Previous CCA applications have proposed various forms of model selection. Christiansen et al. (2009) set d_p and d_t by maintaining a specific level of retained variance in \mathbf{T} and \mathbf{P} and imposing the additional constraint that d_{cca} be equal to the minimum of d_p and d_t . Barnett and Preisendorfer (1987) used principal component truncation rules to determine d_p and d_t as proposed by Preisendorfer et al. (1981). The number of canonical coefficients (d_{cca}) was then estimated using jackknife cross-validation statistics computed for a set of withheld single time samples (“leave one out”). Tippett et al. (2003) employed a similar approach but used a jackknife cross-validation scheme to optimize all three truncation dimensions. Our approach is similar to the latter application, except we use a much cheaper “leave half out” approach to cross validation to reduce computational costs. This procedure produces cross-validation statistics by calibrating independently on either the first or second

halves of the target data and using the left-out half for validation. In an application using proxy data series with annual resolution, this approach is also more conservative with respect to validation of the reconstructed decadal–centennial time scale variations.

To perform the leave-half-out cross-validation procedure, the instrumental period is split into two temporal halves: 1856–1917 and 1918–80 C.E. We generate two sets of reconstructions using (8) and calibrate using each half of the target data to estimate the \mathbf{B}_{cca} matrix, as well as the means and standard deviation fields for the proxy and temperature data ($\mathbf{M}_p, \mathbf{S}_p, \mathbf{M}_t, \mathbf{S}_t$). The reconstructions are verified on the left-out halves of the instrumental data. Two cross-validation statistics are used: 1) the area-weighted root-mean-square error (RMSE) of the reconstructed field relative to the target and 2) the correlation between the reconstructed and target area-weighted mean NH time series [NH mean correlation (NHMC)]. These validation statistics from both experiments are combined to determine the statistics for the entire instrumental data interval from 1856–1980 C.E.

Using the above cross-validation scheme, we compute the RMSE and NHMC for a range of d_{cca} , d_p , and d_t combinations. The optimal selection of d_{cca} , d_p , and d_t is based on the cross-validated reconstruction skill in terms of either small RMSE or large NHMC. After this selection, all matrix parameters of (8) are computed for the entire calibration interval (1856–1980 C.E.) and used for reconstructions in the preinstrumental period. Using the definitions

$$\mathbf{B}_f = \mathbf{S}_t \mathbf{B}_{\text{cca}} \mathbf{S}_p^{-1}, \quad \mathbf{M}_f = \mathbf{M}_t - \mathbf{B}_f \mathbf{M}_p, \quad (9)$$

the reconstruction in (8) can be rewritten in the final form of a linear transform with a constant:

$$\hat{\mathbf{T}} = \mathbf{M}_f + \mathbf{B}_f \mathbf{P}. \quad (10)$$

All columns of the matrix \mathbf{M}_f are identical and specify offsets for all r locations of the predicted temperature fields; therefore, \mathbf{M}_f contains r independent parameters. The linear-transform matrix \mathbf{B}_f has the dimensions $r \times m$ and thus contains $rm = 669 \times 104 = 69\,576$ elements. This number is about one-third smaller than the number of elements in the target temperature data during the calibration period ($rn = 669 \times 125 = 96\,625$) from which the elements of \mathbf{B}_f must be determined. Fortunately, not all elements in \mathbf{B}_f are independent parameters because of the CCA rank reduction. Since \mathbf{B}_{cca} has rank d_{cca} and \mathbf{B}_f is obtained in (9) by multiplying \mathbf{B}_{cca} by nonsingular diagonal matrices, \mathbf{B}_f has the same size ($r \times m$) and rank (d_{cca}) as \mathbf{B}_{cca} . Such a matrix has d_{cca} nonzero singular values and as many left and right singular vectors

corresponding to these values. Using the nonzero singular values of \mathbf{B}_f in nonincreasing order to form a diagonal matrix $\mathbf{\Sigma}$ and arranging the corresponding singular vectors as the columns of matrices \mathbf{U} and \mathbf{V} , we can uniquely (up to the reordering of the columns in \mathbf{U} and \mathbf{V} corresponding to identical singular values) present \mathbf{B}_f as

$$\mathbf{B}_f = \mathbf{U} \mathbf{\Sigma} \mathbf{V}^T. \quad (11)$$

The first column of \mathbf{U} , as a unit vector in the r -dimensional space, has $r - 1$ degrees of freedom. The second column, subject to an additional constraint of orthogonality to the first column, has $r - 2$ degrees of freedom, etc. Therefore, the entire matrix \mathbf{U} , consisting of d_{cca} orthonormal vectors, has

$$\begin{aligned} N(\mathbf{U}) &= \sum_{i=1}^{d_{\text{cca}}} (r - i) = rd_{\text{cca}} - \frac{d_{\text{cca}}(d_{\text{cca}} + 1)}{2} \\ &= d_{\text{cca}} \left(r - \frac{d_{\text{cca}} + 1}{2} \right). \end{aligned}$$

Similarly, the number of independent parameters in \mathbf{V} is

$$N(\mathbf{V}) = d_{\text{cca}} \left(m - \frac{d_{\text{cca}} + 1}{2} \right),$$

and $N(\mathbf{\Sigma}) = d_{\text{cca}}$. In the general case, nonzero singular values of a matrix \mathbf{B}_f are different, the decomposition (11) is unique, and therefore

$$N(\mathbf{B}_f) = N(\mathbf{U}) + N(\mathbf{\Sigma}) + N(\mathbf{V}) = d_{\text{cca}}(r + m - d_{\text{cca}}).$$

Together with the constant offset parameters, the number of independent parameters that have to be determined so as to produce the reconstruction in Eq. (10) is

$$N_{\text{tot}} = N(\mathbf{B}_f) + N(\mathbf{M}_f) = d_{\text{cca}}(r + m - d_{\text{cca}}) + r. \quad (12)$$

Substituting the values of r and m specific to the present pseudoproxy scenario ($r = 669$ and $m = 104$), the number of independent parameters in the CCA temperature field reconstructions are

$$N_{\text{tot}} = 669 + 773d_{\text{cca}} - d_{\text{cca}}^2. \quad (13)$$

The number of independent parameters in the CCA reconstructions therefore depends only on d_{cca} , the number of CCA modes retained. The number does not depend on d_p and d_t , that is, the numbers of retained EOF modes for the proxy and temperature data, respectively. The actual values of \mathbf{B}_f and \mathbf{M}_f in (10), of course, do depend on the d_p and d_t choices, but the underlying number of parameters

that need to be specified to determine these values does not. Furthermore, when $d_{\text{cca}} \ll r + m = 773$, the d_{cca}^2 term in (12) and (13) is negligible compared to $(r + m)d_{\text{cca}} = 773d_{\text{cca}}$. Analyses we will present suggest that reasonable values of d_{cca} are well below 50. Therefore, N_{tot} grows nearly linearly with d_{cca} , and 773 additional parameters need to be specified in the coefficients of (10) when d_{cca} increments by 1. Considering the relative shortness of the dataset available for calibration and cross-validation, choosing a reconstruction model that requires a smaller, rather than larger, number of free parameters (i.e., value of d_{cca}) becomes especially important. In section 4a, we demonstrate a practical means of selecting the smallest d_{cca} that produces a reconstruction with cross-validated RMSE practically indistinguishable from the absolute minimum of RMSE over all combinations of d_{cca} , d_p , and d_r . Thus, the above arguments underlie the dimensional selection strategy that we employ throughout the remainder of the manuscript.

d. RegEM

Application of the RegEM method to the problem of NH CFRs has been discussed in detail within the literature (Schneider 2001; Rutherford et al. 2005, 2010; Mann et al. 2005, 2007a,c, 2008; Smerdon and Kaplan 2007; Lee et al. 2007; Smerdon et al. 2008b; Riedwyl et al. 2009; Christiansen et al. 2009, 2010; Tingley and Huybers 2010a,b). Although RegEM is an iterative method, the underlying formalism is based on a linear regression model that, for a given time step, reconstructs missing data \mathbf{X}_m from available data \mathbf{X}_a and can be written as

$$\mathbf{X}_m = \mathbf{M}_m + \mathbf{S}_m \mathbf{B} \mathbf{S}_a^{-1} (\mathbf{X}_a - \mathbf{M}_a). \quad (14)$$

The notation here is analogous to (3), except the subindices a and m denote available and missing data, respectively, and are consistent with the notation adopted by Schneider (2001).

For the conventional expectation maximization (EM) algorithm, in which regularization is not employed, the estimate of the regression matrix \mathbf{B} is given, in full analogy to (2), by the standard multivariate regression formula for standardized datasets X'_m and X'_a :

$$\mathbf{B} = (\mathbf{X}'_m \mathbf{X}'_a{}^T) (\mathbf{X}'_a \mathbf{X}'_a{}^T)^{-1}. \quad (15)$$

Similar to CCA, however, regularization is required for application to CFRs of the last millennium. Multiple regularization approaches for the expectation maximization algorithm have been discussed (Schneider 2001; Rutherford et al. 2005, 2010; Mann et al. 2005, 2007a,c; Smerdon and Kaplan 2007; Christiansen et al. 2009,

2010), but the differences between reconstructions derived from these approaches have not been sufficiently explored (Smerdon et al. 2008b). For our purposes herein we employ the more widely applied ridge regression regularization, in which the inverse covariance matrix in (15) is replaced by

$$(\mathbf{X}'_a \mathbf{X}'_a{}^T)^{-1} \rightarrow (\mathbf{X}'_a \mathbf{X}'_a{}^T + h^2 \mathbf{I})^{-1}, \quad (16)$$

where h is a positive number called the ridge parameter (see Schneider 2001 for a detailed derivation and discussion of these equations). In keeping with the reconstructions performed by Rutherford et al. (2005) and Mann et al. (2005), h is chosen herein by minimization of the generalized cross validation (GCV) function. In general, the RegEM algorithm allows the set of missing data locations to vary arbitrarily with time, thus making all matrices appearing in (14) time variable. Nevertheless, in cases where the missing values in the data matrix take the form of a block submatrix (i.e., \mathbf{X}_m now denotes the estimate for this submatrix and \mathbf{X}_a is a submatrix of available data for the time period corresponding to \mathbf{X}_m), the final RegEM reconstruction takes the form of (14) for a simple specific choice of \mathbf{M}_a , \mathbf{S}_a , \mathbf{M}_m , \mathbf{S}_m , and \mathbf{B} (Smerdon et al. 2008b)—such is the case in the present millennial CFR context. Moreover, if the proxy data in \mathbf{P} are substituted for the available data \mathbf{X}_a and the missing data \mathbf{X}_m are taken to be temperature \mathbf{T} during the reconstruction interval, then the RegEM reconstruction in (14) essentially becomes (3) and is comparable to the same form given for the CCA reconstruction in (8). In fact, both of these reconstruction formulas can be brought to the form in (10) that uses one offset and one matrix transformation.

The main difference between (8) and (14)–(16) is of course the form of regularization used for the regression matrix \mathbf{B} and the iteratively computed estimates of RegEM. Several relative advantages of the RegEM method using ridge regression regularization (RegEM-Ridge) have been noted (Schneider 2001). In typical climatological applications where only a few principal components are retained based on often weak separations of the leading elements in the eigenvalue spectrum, the continuous filtering of the spectrum in ridge regression may provide advantages over regularizations, like CCA, that use finite eigenvalue truncation. The iterative EM procedure also allows the use of all data in the data matrix, as opposed to only the predictand and predictor data during their period of overlap in the calibration interval. In the specific type of paleoclimatic application considered herein, however, this advantage is limited principally to the precalibration period of the proxy matrix because the target data are completely

TABLE 1. Early (1856–1917 C.E.) and late-half (1918–80 C.E.) cross-validation statistics for CCA; all statistics and dimensions represent those achieved for the minimum RMSE in the two respective cross-validation periods.

SNR	Early-half calibration					Late-half calibration				
	RMSE	d_{cca}	d_p	d_t	NHMC	RMSE	d_{cca}	d_p	d_t	NHMC
Infinity	0.54	19	24	39	0.84	0.58	16	33	30	0.77
1.0	0.62	16	23	21	0.57	0.65	16	24	20	0.64
0.5	0.70	10	40	19	0.54	0.71	7	26	11	0.53
0.25	0.74	9	40	39	0.21	0.76	3	48	32	-0.02

missing prior to the mid-nineteenth century (cf. Smerdon et al. 2008b).

4. Reconstruction results

a. Selected model dimensions

We select d_{cca} , d_p , and d_t values for the collection of CCA reconstructions that calibrate the 104 pseudo-proxies on the instrumental period from 1856–1980 C.E. and compute CFRs during the interval 850–1855 C.E. In all cases, \mathbf{P} and \mathbf{T} are standardized over the calibration period prior to estimating the regression matrix \mathbf{B}_{cca} using Eq. (7); reconstructions during the validation period are performed using (8).

Following the approach described in section 3c, the CCA model was calibrated on each half of the instrumental data and tested on the other half using all combinations of d_{cca} , d_p , and d_t between 1 and 50 modes such that $d_{cca} \leq \min(d_p, d_t)$ [yielding d_{cca}^2 triplets (d_{cca} , d_p , d_t) for each d_{cca} value between 1 and 50 and thus a total of $1^2 + 2^2 + \dots + 50^2 = 50(50 + 1)(2 \times 50 + 1)/6 = 42\,925$ reconstruction models]. The cross-validation statistics for early and late calibration halves are given in Table 1. These results for both halves of the instrumental period were combined to produce cross-validation statistics for the entire interval and a given set of dimensions. RMSE values were combined as the square root of the mean residual sum of squares in the two intervals, and NHMCs were calculated as the average correlation coefficients for the two intervals.

Table 2 gives the minimum RMSE and maximum NHMC values among all d_{cca} , d_p , and d_t combinations used, as well as the dimensional combinations that achieve these extrema. Results are tabulated for each pseudo-proxy noise level. Although the two statistics are optimized at somewhat similar dimensional combinations, the results are not identical—the alternative statistic for each optimization is also provided in Table 2.

The RMSE and the NHMC statistics are plotted in Fig. 2 for an SNR of 0.5, showing that the former generally

TABLE 2. CCA reconstruction statistics using the absolute minimum RMSE or maximum NHMC criteria during the calibration interval (1856–1980 C.E.).

SNR	Absolute minimum RMSE					Absolute maximum NHMC				
	RMSE	d_{cca}	d_p	d_t	NHMC	RMSE	d_{cca}	d_p	d_t	NHMC
Infinity	0.57	22	35	46	0.77	0.59	25	29	50	0.83
1.0	0.64	15	23	20	0.59	0.69	16	37	47	0.67
0.5	0.71	6	22	10	0.52	0.74	5	21	26	0.61
0.25	0.76	3	30	4	0.26	0.79	6	50	48	0.33

decreases as the latter increases. More importantly, the range of possible NHMCs decreases as the RMSE becomes smaller. The reciprocal constraint, however, is much weaker: increases in NHMCs are not accompanied by nearly as large a decrease in the range of RMSE. This suggests that RMSE is a more robust statistic for optimizing the CCA reconstructions than the NHMC. Furthermore, the colors of the circles in Fig. 2 denote the values of d_{cca} , that is, they correspond to the number of independent parameters in the reconstruction model that is being validated. While particularly small d_{cca} (less than 10) correspond to reconstructions that are both poor in RMSE and NHMC performance, high d_{cca} (larger than 30) correspond to high NHMC but the full range of RMSE values. RMSE performance is especially poor for reconstructions with the largest d_{cca} values. We therefore use RMSE as the principal basis for our selection criterion in subsequent dimensional selections. There are of course alternative cross-validation statistics that could be

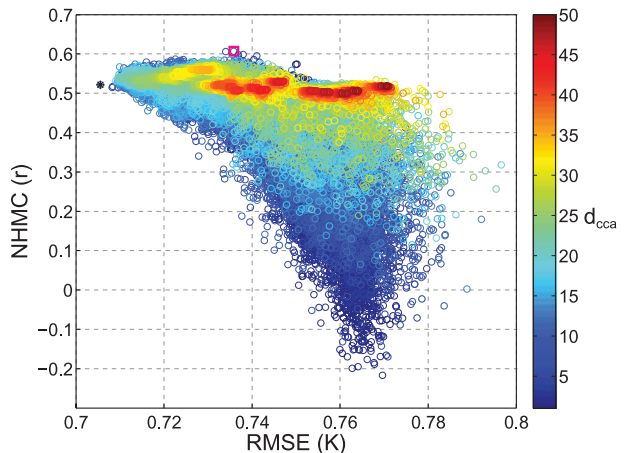


FIG. 2. Cross-validation statistics during the calibration interval (1856–1980 C.E.) for the ensemble of CCA reconstructions at an SNR of 0.5. Colors in the figure indicate the value of d_{cca} , which ranges from 1 to 50. The symbols in the figure correspond to the following CCA solutions: the absolute minimum RMSE (black dot), the maximum NHMC (pink square), and the preferred solution based on RMSE (black star), which overlays the black dot for this particular noise realization.

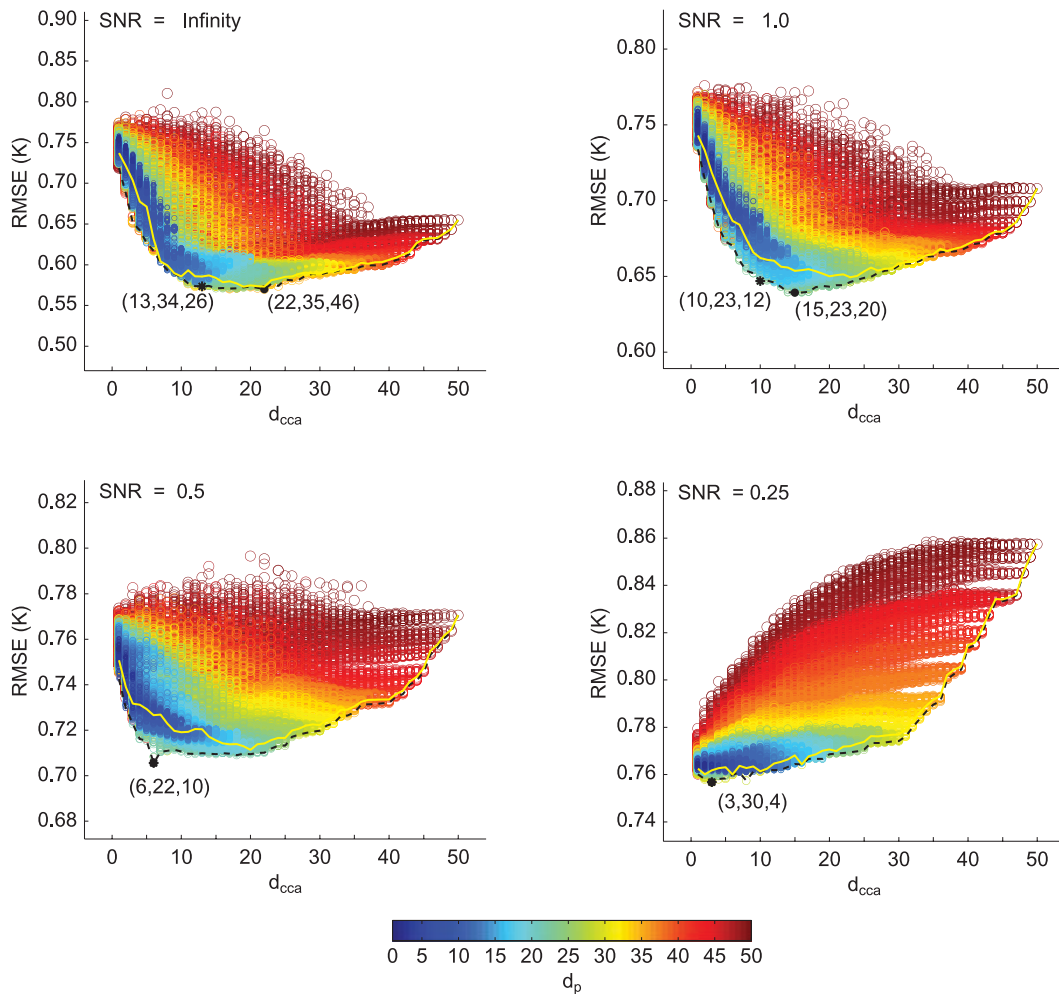


FIG. 3. RMSE as a function of d_{cca} for all reconstructions spanning the collection of dimensional combinations between 1 and 50. Colors in the figure indicate the value of d_p chosen for the derived RMSE value. Yellow lines in each of the RMSE plots indicate the minimum RMSE achieved when d_t is held constant at 50. Black dots correspond to the absolute minimum RMSE and the values of d_{cca} , d_p , and d_t are given in the parentheses next to each dot. The locations of the preferred solutions based on RMSE are also shown with a black star; the dimensional combinations for these values are also given in parentheses.

adopted. The coefficient of efficiency (CE) and reduction of error (RE) statistics are often used in paleoclimate literature as statistical validation measures. Advocates of these statistics point out that RE and CE measure the robustness of both the resolved variance and reconstructed mean in derived reconstructions (e.g., Wahl and Ammann 2007). This advantage is shared by the RMSE statistic adopted in this study, indicating that all three skill measures would be expected to produce similar results. Nevertheless, we adopt RMSE in the present application given its readily interpretable characteristics.

As mentioned earlier, the total number of combinations used to determine the optimized dimensions given in Table 2 is 42 925. This collection of models was tested for their cross-validated performance on only 125 annual

fields of target data, thus some combinations might correspond to low RMSE simply by chance and yield optimal reconstructions impacted by artificial skill. To guard against this likelihood, we adopt a conservative selection strategy that seeks to find the most parsimonious of acceptable models by minimizing the number of free parameters in the final reconstruction model, which is equivalent to minimizing d_{cca} without deviating significantly from the absolute minimum RMSE. Figure 3 plots RMSE versus d_{cca} for all tested combinations of the CCA dimensions at each pseudoproxy noise level; the black dashed line connects the RMSE minima for each value of d_{cca} :

$$\text{RMSE}^*(d_{cca}) = \min_{d_p, d_t} \text{RMSE}(d_{cca}, d_p, d_t).$$

TABLE 3. CCA reconstruction statistics for the preferred solutions in which parsimonious dimensional combinations have been chosen as the first local minimum of the RMSE statistic.

SNR	Preferred solutions				NHMC
	RMSE	d_{cca}	d_p	d_t	
∞	0.57	13	34	26	0.74
1.0	0.65	10	23	12	0.60
0.5	0.71	6	22	10	0.52
0.25	0.76	3	30	4	0.26

If $d_p^*(d_{cca})$ and $d_t^*(d_{cca})$ are the values of d_p and d_t that respectively minimize $RMSE(d_{cca}, d_p, d_t)$ for a given d_{cca} , then the triplet $(d_{cca}, d_p^*(d_{cca}), d_t^*(d_{cca}))$ defines the optimal (by the cross-validated RMSE criterion) CCA reconstruction among all models with a fixed number of independent parameters. Figure 3 demonstrates that $RMSE(d_{cca})$ decreases steeply for all noise levels at small values of d_{cca} . Beginning at a given d_{cca} value, however, this drop is replaced by a rather flat plateau. For all noise levels except the highest one, the absolute minimum (identified by the closed circle) is rather far from the beginning of this plateau. Alternatively, using the d_{cca} value corresponding to the beginning of the plateau yields a solution with an RMSE performance that is similar to the absolute RMSE minimum but corresponds to a model with a much smaller number of independent parameters.

We identify the beginning of the plateau by selecting the minimum d_{cca} at which an increase by one does not reduce $RMSE^*(d_{cca})$:

$$d_{cca}^* = \min[d_{cca} : RMSE^*(d_{cca}) \leq RMSE^*(d_{cca} + 1)].$$

Optimal solutions $[d_{cca}^*, d_p^*(d_{cca}^*), d_t^*(d_{cca}^*)]$ are identified by stars in the panels of Fig. 3 and are listed in Table 3 along with the corresponding values of RMSE and NHMC cross-validation statistics. At any noise level, $RMSE^*(d_{cca}^*)$ does not exceed $\min_{d_{cca}}(RMSE^*)$ by more than 1.5%. In subsequent presentations herein, we use these “beginning of the plateau” solutions $[d_{cca}^*, d_p^*(d_{cca}^*), d_t^*(d_{cca}^*)]$ as our preferred choices of the CCA dimensions (termed the preferred solutions hereafter).

Note that in the preferred solutions the values of d_p and d_t are chosen as those corresponding to the absolute minimum of RMSE for the preselected value of d_{cca} . Relatively fluid color transitions in the panels of Fig. 3 suggest smooth but significant dependence of RMSE on d_p . This impression is borne out in a more detailed illustration of the RMSE dependence on the CCA parameters (d_{cca}, d_p, d_t) : Fig. 4 presents two-dimensional fields of the RMSE minima with respect to the individual dimensions for a SNR = 0.5. The area of the RMSE minimum is quite wide, therefore, changes in d_p or d_t by a few units should not affect the reconstruction quality very much. The dependence of RMSE on d_t is particularly poorly constrained by the data; for all d_{cca} in the range between 5 and 30, a value of d_p could be selected so that RMSE is quite close to the absolute minimum for any value of d_t exceeding d_{cca} . Nevertheless, reductions in the dimensions of the temperature field are warranted. The yellow lines in Fig. 3 plot the minimum

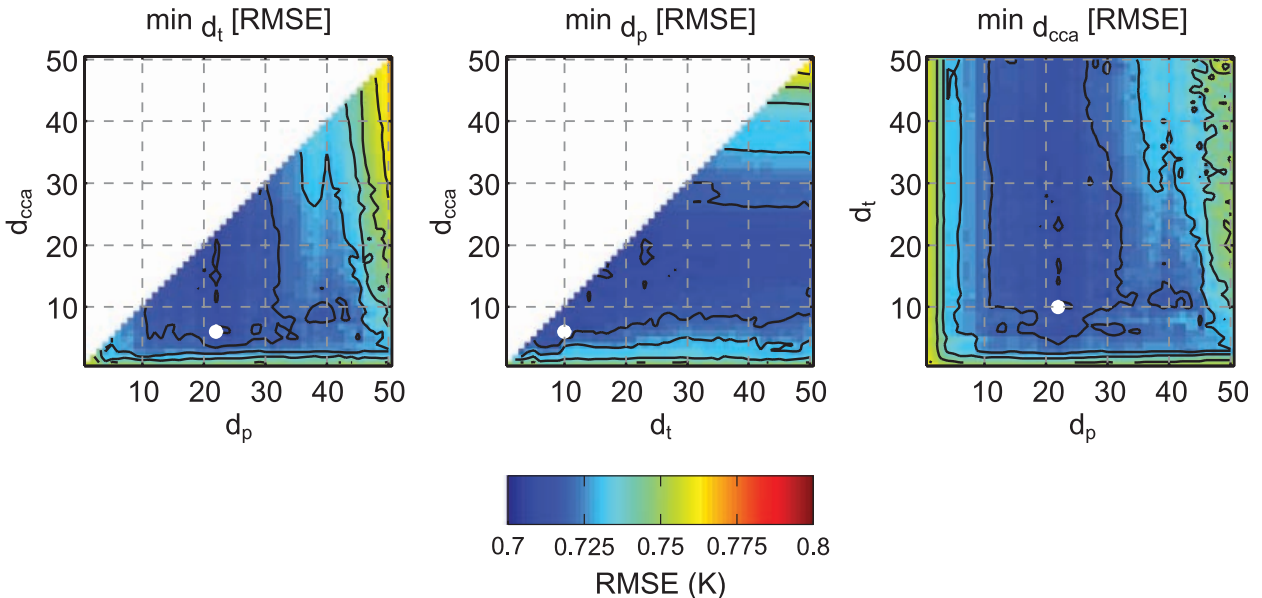


FIG. 4. Minimum RMSE values for each pairing of the d_{cca} , d_p , and d_t dimensions at an SNR of 0.5. The absolute minimum RMSE value is plotted as a white dot; the preferred solution value is plotted as a white star (which overlays the white dot for this particular noise realization).

RMSE values in the subset of solutions when d_t is held constant at 50 (close to 62 or 63, the full rank of the temperature field in the two halves of the instrumental period). At all noise levels, the preferred solutions display reduced RMSE when the dimension of the temperature field is truncated. Moreover, in real-world reconstructions, which involve predictand fields that contain noise or calibration intervals that can be shorter than the ones used herein, improvements in calibration errors due to the reduction of the predictand matrix would likely be more significant (Bretherton et al. 1992).

b. CCA reconstructions

1) ASSEMBLY OF THE CCA RECONSTRUCTIONS

To demonstrate the individual elements of the CCA reconstruction, we plot in Fig. 5 the homogeneous covariance maps (C_t and C_p) and the associated time series (Q_t) for the first three canonical patterns of the no-noise reconstruction (see section 3b and Appendix A). In the case of Q_t , we plot both the true time series from the target data, as well as the estimated time series from the pseudoproxy matrix ($\Sigma_{cca} \mathbf{Q}_p^T$).

The three temperature covariance maps plotted in Fig. 5 take on dynamically interpretable characteristics representing the variability in the CCSM versions of the global (hemispheric) mean, the North Atlantic Oscillation, and the El Niño–Southern Oscillation, respectively. This demonstration illustrates the physical interpretability of the derived covariance maps, which ultimately can be evaluated in terms of the reconstruction skill associated with individual dynamical patterns in the field.

As demonstrated in step (ii) of the 3-step procedure in section 3b, the time series of the temperature covariance maps are estimated during the reconstruction interval by the product of the canonical coefficients and the time series of the proxy covariance maps. These time series are plotted in Fig. 5 and compare closely to the true time series of the temperature covariance maps. Correlations between the true and estimated time series for these first three patterns are all above 0.99 in the calibration interval and above 0.98 in the reconstruction interval (see Table 4 for these statistics at all noise levels). As dictated by the CCA formulation, correlations within the calibration interval progressively decrease from the maximum of the first pattern for all noise levels (Table 4). This is interestingly not the case in the reconstruction interval when some of the correlations for higher-order patterns exceed those of the lower-order patterns.

Figure 5 also plots the relative values of the proxy covariance maps for the first three canonical patterns. These maps scale location markers for the 104 pseudoproxies by their relative loadings and also designate

where the loadings are positive or negative using the color of the markers. Upon inspecting the two sets of temperature and pseudoproxy covariance maps one can see that the proxy maps effectively reflect local sampling from the temperature maps. For instance, the leading canonical pattern associated with predominant warming is reflected in the proxy map that contains nearly all positive loadings. In the other two patterns, the positive and negative loadings are roughly collocated with the areas of positive and negative temperature anomalies in the temperature covariance maps. These maps also indicate relatively balanced loadings of the pseudoproxies in which no single record is weighted heavily in a given pattern. Equivalent maps in real-world CFR applications would similarly be useful for evaluating the impact of specific proxies in the derived reconstructions.

2) NORTHERN HEMISPHERE MEANS

Corresponding temperature covariance maps and proxy-estimated time series as represented in Fig. 5 are combined to yield a complete field reconstruction for each of the investigated noise levels. The total number of combined patterns is of course dictated by the number of retained d_{cca} values, which were determined for the preferred solutions in section 4a to range from 13 in the no-noise case to 3 at an SNR of 0.25 (see Table 3). Complete CCA reconstructions are assembled from these collections of patterns and time series. We first plot the area-weighted mean NH time series associated with these complete reconstructions in Fig. 6a.

The correlations between the reconstructed mean NH time series and the model target are all significant, even though they reduce with increasing noise levels (Table 5). These correlations are interestingly less than those determined for the first three canonical patterns at all noise levels given in Table 4. This is indicative of the fact that the leading individual patterns are reconstructed more skillfully than the mean of the combined field containing the full range of scaled canonical patterns.

Although the determined correlations are all significant, the time series in Fig. 6a suffer from warm biases and variance losses during the reconstruction interval, both of which increase with higher noise levels. This behavior is not associated with the difference between the dimensions chosen for the preferred solutions in section 4a and those for the absolute minimum RMSE—Fig. 6b plots the mean time series from the reconstructions using the latter-derived dimensions and the results still suffer from the observed effects. These absolute-minimum time series correlate with the preferred solution reconstructions at levels of $r = 0.98$ or better during the reconstruction interval. The robustness of the achieved results and the prevalence of the observed warm biases and

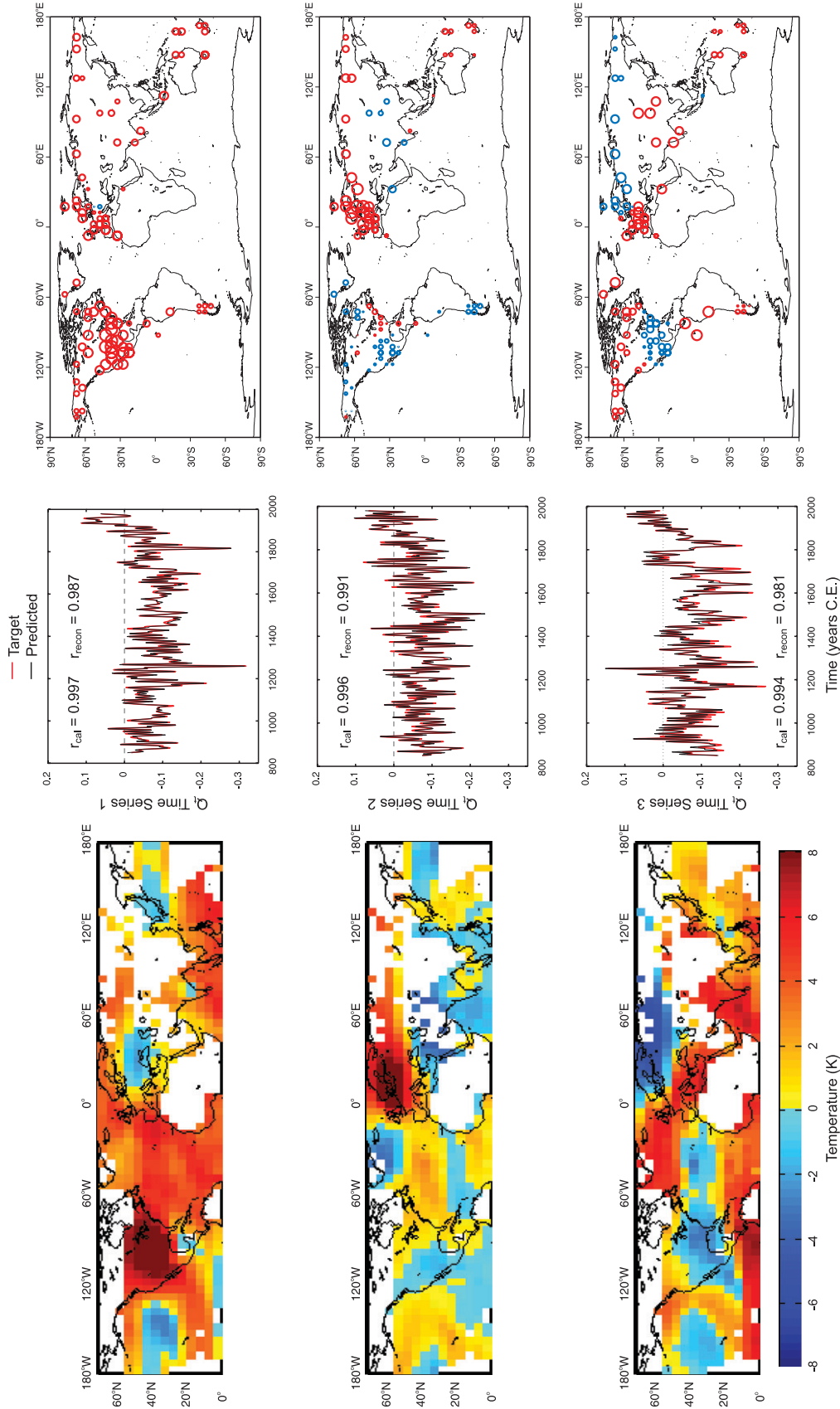


FIG. 5. (left) Temperature homogeneous covariance maps (\mathbf{C}_T), (middle) target and predicted time series of the temperature maps (Q_i and $\Sigma_{\text{cat}} \mathbf{Q}_i$), and (right) proxy homogeneous covariance maps (\mathbf{C}_P) for the first three canonical patterns of the no-noise reconstructions (rank increases from the top to bottom). The circles in the proxy maps represent the loadings for each pattern, where blue and red circles correspond to positive and negative loadings, respectively, and the circle areas are proportional to the loading magnitude. All elements are estimated over the calibration interval, but the time series are extended into the reconstruction interval by projecting the covariance maps onto the temperature and proxy matrices over the full temporal period. Correlations between the target and predicted time series during the calibration and reconstruction intervals are given in the middle column. The percentage of variance explained in the target field during the calibration interval are 11.6%, 4.5%, and 9.8% by the first, second, and third covariance maps, respectively.

TABLE 4. Correlation statistics between the true canonical temperature time series Q_t and those predicted by the proxy PCs, that is, $\Sigma_{cca} \mathbf{Q}_p^T$. Statistics are shown for both the reconstruction (Recon) and calibration (Cal) intervals.

CCA rank	SNR infinity		SNR 1.0		SNR 0.5		SNR 0.25	
	Cal	Recon	Cal	Recon	Cal	Recon	Cal	Recon
1	0.997	0.987	0.956	0.909	0.901	0.831	0.734	0.399
2	0.996	0.991	0.938	0.915	0.849	0.707	0.688	0.430
3	0.994	0.981	0.914	0.868	0.801	0.599	0.577	0.266
4	0.992	0.963	0.908	0.835	0.764	0.412	—	—
5	0.986	0.953	0.828	0.706	0.678	0.655	—	—
6	0.969	0.891	0.797	0.421	0.659	0.347	—	—
7	0.959	0.904	0.768	0.635	—	—	—	—
8	0.953	0.919	0.651	0.573	—	—	—	—
9	0.948	0.888	0.619	0.519	—	—	—	—
10	0.933	0.777	0.473	0.273	—	—	—	—
11	0.915	0.822	—	—	—	—	—	—
12	0.905	0.792	—	—	—	—	—	—
13	0.853	0.654	—	—	—	—	—	—

variance losses in the NH means are thus illustrated by the strong similarities between Figs. 6a and 6b. Local correlations also reflect a strong consistency between the absolute minimum and preferred reconstructions: the area-weighted mean field correlations from 850–1855 C.E. between the two reconstructions are 0.92 and 0.97 for SNR = infinity and 1.0, respectively. (Note that the dimensional selections for the SNR = 0.5 and 0.25 cases

were the same for both the absolute minimum and preferred solutions, thus no correlation statistics are necessary for those noise levels.) These comparisons demonstrate a spatial consistency between the two dimensional choices and suggest that the large-scale features are well captured for different sets of CCA dimensions (assuming the RMSE is held close to the absolute minimum).

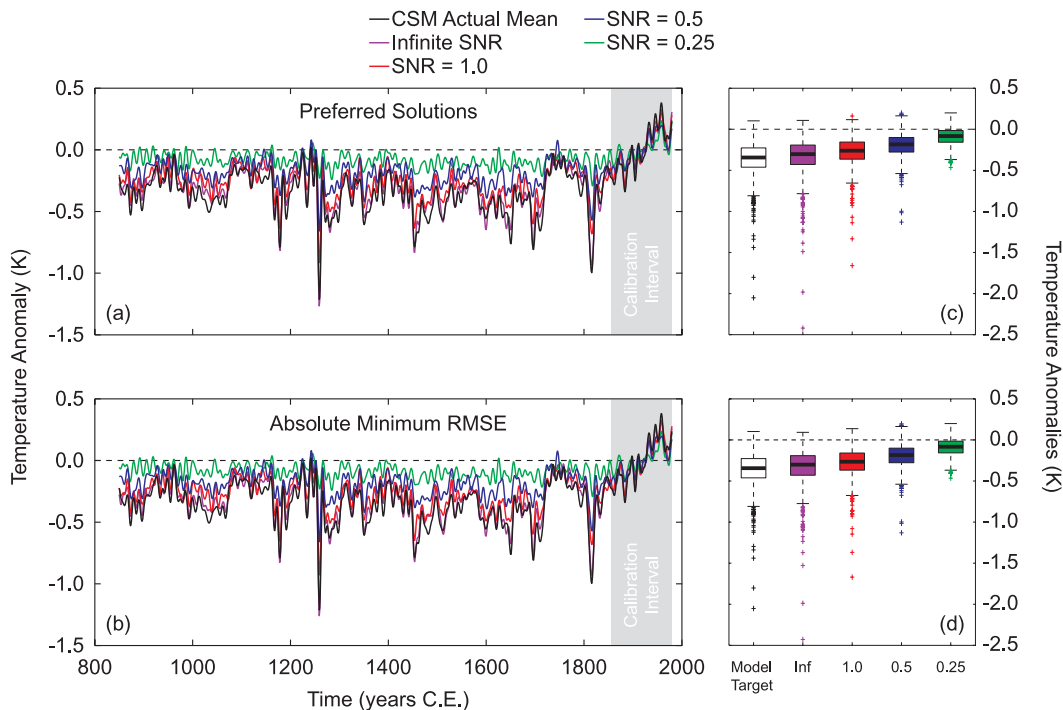


FIG. 6. Area-weighted NH time series for the CCA reconstructions using d_{cca} , d_p , and d_t values associated with: (a) the preferred solution (Table 3) and (b) the absolute minimum RMSE values (Table 2). Time series have been smoothed using a decadal low-pass filter. (c),(d) The box plots associated with the two combinations of the of d_{cca} , d_p , and d_t values. These plots were calculated from the distribution of the individual annual means in each NH time series during the reconstruction interval.

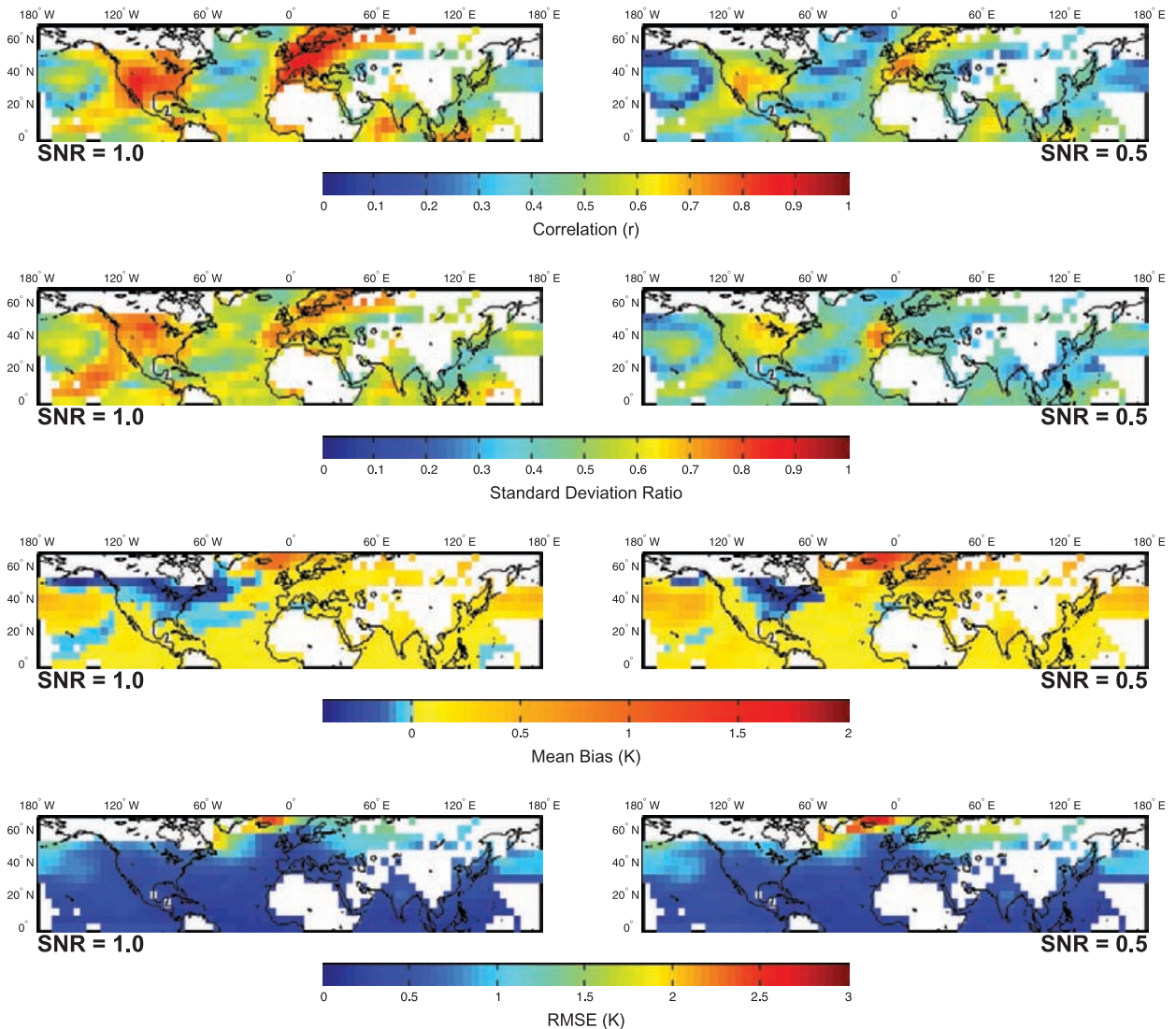


FIG. 7. Field comparisons between derived CCA reconstructions (using the preferred solution values of d_{cca} , d_p , and d_t) and the known CCSM model field: (top) correlation, (second row) standard deviation ratios, (third row) mean biases, and (bottom) RMSE. Standard deviation ratios are computed between the reconstruction and model, and mean biases are computed as reconstruction minus model, that is, negative (positive) biases indicate a colder (warmer) reconstruction mean. Results are shown for SNRs of (left) 1.0 and (right) 0.5. Summary statistics for all noise levels are given in Table 4. All statistics are computed over the reconstruction interval (850–1855 C.E.).

The box plots in Figs. 6c and 6d are calculated from the distribution of the individual annual means in each NH time series during the reconstruction interval. The plots further demonstrate the warm biases and variance losses in the reconstructed NH time series, as well as the reduced number of extreme events in the reconstructed time series relative to the known model target. These extrema are typically associated with volcanic events in the model-simulated NH mean, and are manifest as cold outliers in both the model target and the reconstructed time series. The number and extent of the outliers is diminished in the reconstructed time series, however, and indicates that the reconstructions have the potential

to miss the characterization of these important annual events in the model-simulated climate.

3) RECONSTRUCTED FIELDS

Figure 7 shows the spatial distributions of validation statistics for the preferred CCA reconstructions at SNRs of 1.0 and 0.5; statistics are computed during the reconstruction interval and summary statistics for all noise levels are given in Table 5. Field correlations of course reduce with increased noise, but Fig. 7 illustrates the spatial variability of the local correlation coefficient. In all reconstructions, regions containing the largest correlations are over North America and Europe. These regions

TABLE 5. Validation statistics computed during the reconstruction interval (850–1855 C.E.) for the CCA and RegEM-Ridge reconstructions. Reconstructions from each method were derived with the same set of pseudoproxies at all noise levels. All field statistics were weighted by the cosine of the midlatitude for each grid cell.

SNR	NHMC	Mean field correlation	Mean STD ratio	Mean bias (K)	Mean RMSE (K)
CCA					
∞	0.91	0.70	0.77	0.03	0.49
1.0	0.84	0.58	0.58	0.09	0.59
0.5	0.76	0.44	0.44	0.17	0.67
0.25	0.43	0.23	0.29	0.27	0.77
RegEM-Ridge					
∞	0.91	0.68	0.52	−0.01	0.52
1.0	0.85	0.60	0.38	0.11	0.60
0.5	0.78	0.47	0.24	0.20	0.69
0.25	0.49	0.24	0.15	0.28	0.76

correspond to the areas with the largest density of pseudoproxies (see Fig. 1), that is, the reconstructions perform best where the field is sampled the most. Similarly, regions that are not sampled in the pseudoproxy network have comparatively low verification correlations. Correlations fall to particularly low values over some important regions (e.g., subtropical and midlatitude ocean basins or the Asian continent) at high-noise levels.

The warm biases and variance losses observed in the mean NH time series (Fig. 6) are also manifest in the reconstructed fields, but their spatial patterns show important regional distinctions (Fig. 7). Standard deviation ratios (sample standard deviation of the reconstruction divided by the corresponding model value) indicate that variance is most strongly preserved in areas where field correlations are high, whereas variance losses are largest over the ocean basins where the lowest field correlations are observed; note that, although standard deviation ratios expressed in this manner cannot serve as a reasonable estimate of the system variance, they do serve as a convenient measure of the skill of the reconstruction (Smerdon et al. 2008b). Overall, significant variance losses are observed for all noise levels: the area-weighted mean standard deviation ratio is respectively 0.58 and 0.44 for the SNR cases of 1.0 and 0.5 shown in Fig. 7, whereas the ratio drops to 0.29 at a SNR of 0.25 (Table 5). Additionally, large variance losses can accompany reconstructions with relatively high correlations in the field: standard deviation ratios drop below 0.5 in many regions of the reconstruction for an SNR of 1.0 (Fig. 7).

Mean biases also display regional variations, although they appear more spatially uniform than observed for the local correlations or standard deviation ratios. Although most regions of the reconstructions are warmer than the actual model field, means are colder in a few areas (e.g., North America and parts of the Pacific and Atlantic Oceans). The proportion of colder to warmer regions is

reduced with increasing noise levels and is reflected in the average mean biases calculated for the fields (see Table 5); therefore, high-noise reconstructions are dominated by warm-biased regions.

The bottom panels in Figure 7 show the RMSE of the fields, which combine errors associated with variance losses and mean biases. The RMSE patterns follow most closely the patterns in the mean biases, indicating that the error is dominated by differences between the reconstructed and actual means. Contrary to the correlation patterns, it is also important to note that the RMSE is in some cases largest over regions where the pseudoproxy network is densest. Mean biases, and therefore RMSE, do not appear to be as strongly tied to the distribution of the pseudoproxy network as the correlation and standard deviation ratios.

c. Comparison of CCA and RegEM reconstructions

We have used the same pseudoproxies from the above CCA experiments to compute corresponding nonhybrid (Rutherford et al. 2005) RegEM-Ridge reconstructions. The derived reconstructions employ a standardization scheme realistically confined to the calibration interval (Smerdon and Kaplan 2007) during which no detrending has been applied—all reconstructions have used a stagnation tolerance of 5×10^{-4} . Figures 8a and 8b compare the mean NH time series computed from the CCA and RegEM-Ridge reconstructed fields at SNRs of 1.0 and 0.5. The time series at all noise levels compare very closely, as reconstruction interval correlations between the CCA and RegEM-Ridge time series are 0.94, 0.98, 0.97, and 0.87 for SNR = ∞ , 1.0, 0.5, and 0.25, respectively. The reconstructed NH means also correlate with the true model mean at comparable levels (Table 5). There is, however, an indication that the RegEM-Ridge method performs slightly better given that the correlations increase by a few hundredths above those observed

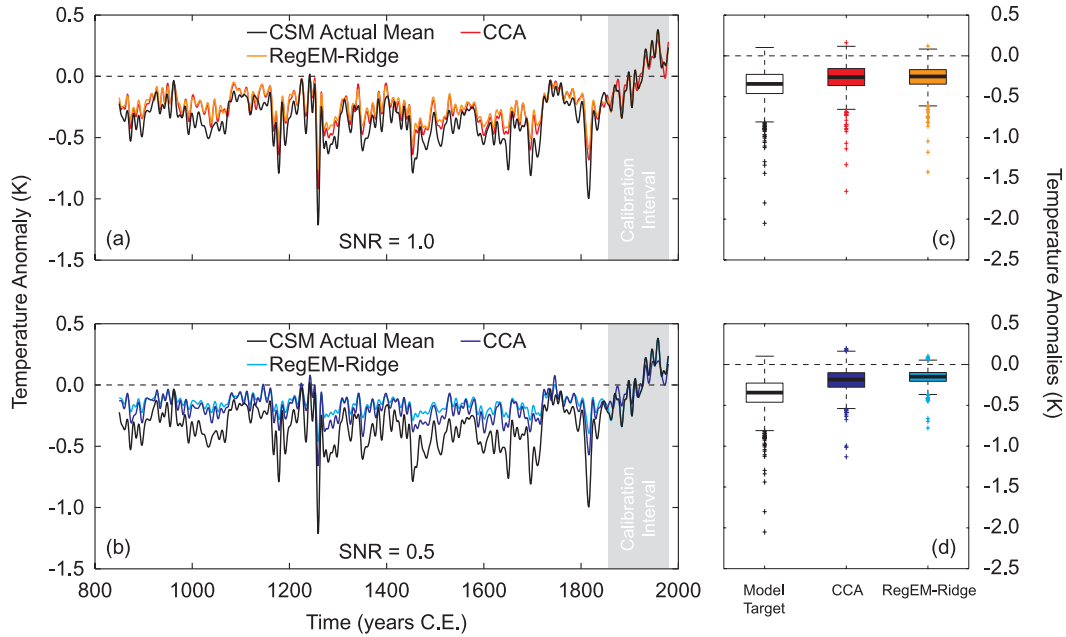


FIG. 8. As in Fig. 6 but for comparisons between the area-weighted NH time series for CCA and RegEM-Ridge reconstructions. Results are shown for SNRs of 1.0 and 0.5. Summary statistics for all noise levels are given in Table 5.

for CCA. The variance losses are larger in the RegEM-Ridge reconstructions, however, and can be clearly seen in the box plots in Figs. 8c and 8d. These losses are also manifest in the failure to reconstruct extreme events, which is also slightly more apparent in the RegEM-Ridge reconstructions as illustrated in the latter panels of Fig. 8.

The correlation fields between the CFRs derived from the two methods are plotted in Fig. 9, again showing results for SNRs of 1.0 and 0.5. Correlations between the two reconstructions depend on location, but overall the area-weighted mean field correlations in the reconstruction interval are 0.89, 0.91, 0.84, and 0.61 for SNR = ∞, 1.0, 0.5, and 0.25, respectively. As discussed in section 3, CCA and RegEM-Ridge select regression coefficients in two distinctly different ways; however, the widespread high field correlations between the results from both methods

indicate that they reconstruct similar patterns of variability in the target field (note that the exact same pseudoproxies have been used for each of these experiments).

Validation fields for the RegEM-Ridge reconstructions are shown in Fig. 10. These are directly comparable to the CCA validation fields shown in Fig. 7. The close correspondence between the two figures further attests to the similarities between the results derived from both methods. Summary statistics for the RegEM-Ridge field correlations, standard deviation ratios, mean biases, and RMSE are given in Table 5. The mean field correlations associated with the two methods are very similar, yet indicate RegEM-Ridge to have slightly more correlation skill at increased noise levels. The RegEM-Ridge mean biases also have spatial patterns very similar to CCA but indicate that RegEM-Ridge produces larger biases at increased noise levels. The most notable difference between

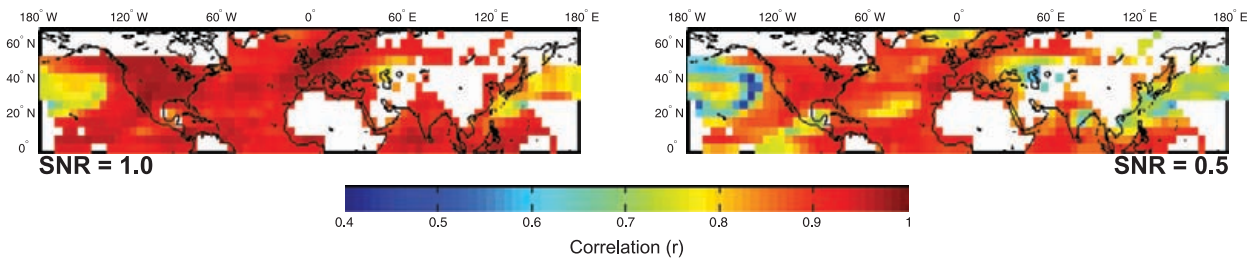


FIG. 9. Correlation fields between the CCA and RegEM-Ridge reconstructions. Results are shown for SNRs of (left) 1.0 and (right) 0.5 and are computed over the reconstruction interval (850–1855 C.E.).

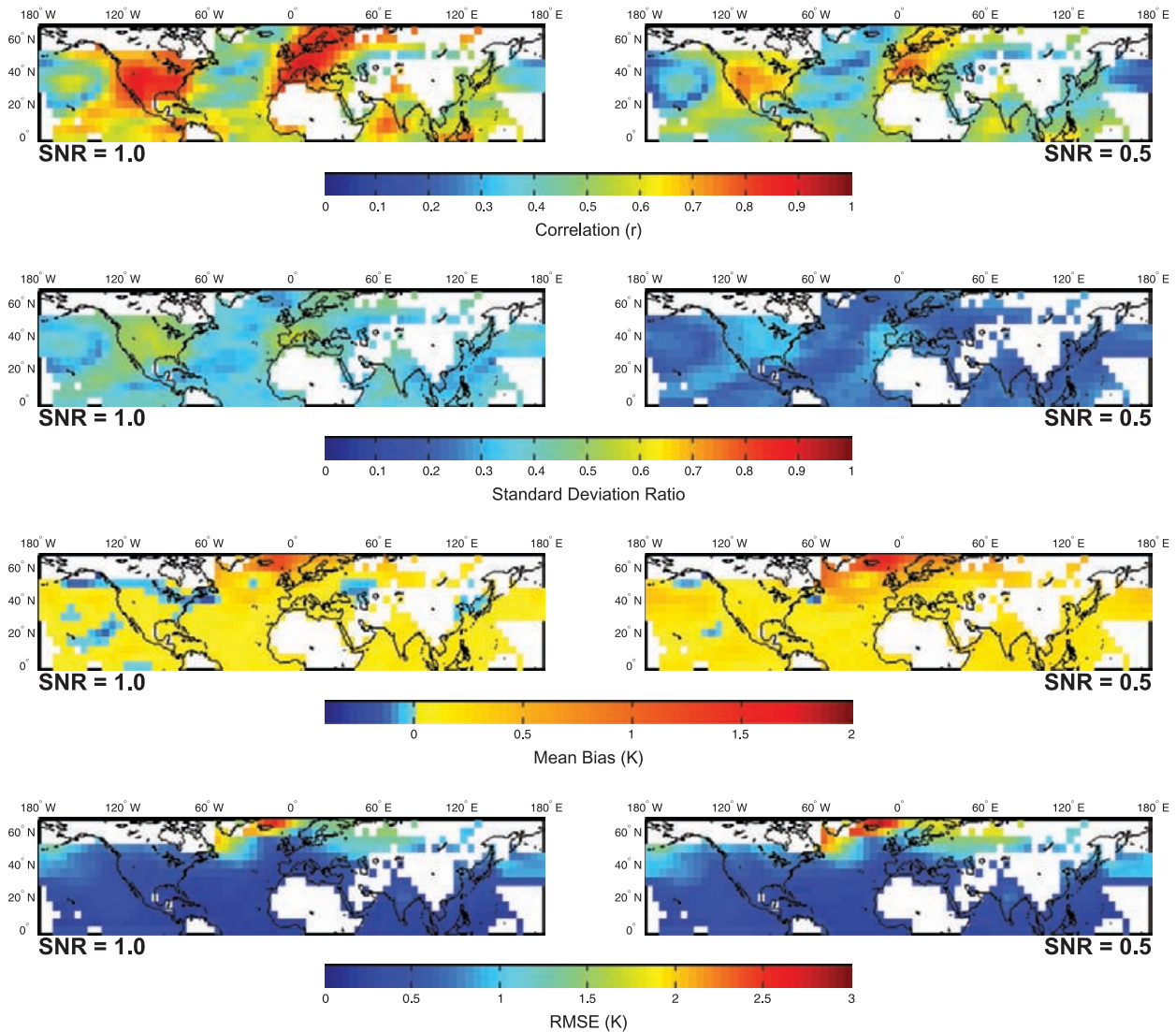


FIG. 10. As in Fig. 7 but for the RegEM-Ridge reconstructions.

the two methods is associated with their standard deviation ratios. RegEM-Ridge standard deviation ratios have patterns similar to the CCA reconstructions and also maintain the most variance where the field correlations are highest. The variance loss in RegEM-Ridge, however, is much more pronounced than in the CCA reconstructions: mean standard deviation ratios are only 68% of those achieved for the CCA reconstructions at a SNR of infinity and fall to 52% of the CCA counterpart at a SNR of 0.25. These variance losses are manifest in the higher RMSE values associated with the RegEM-Ridge fields, but they result in only modest increases in the mean field errors (Table 5) relative to CCA. Two factors contribute to the similar RMSE fields in spite of the larger variance losses in the RegEM-Ridge CFRs: 1) the mean biases dominate the error fields and 2) the slightly higher

correlations associated with the RegEM-Ridge reconstructions offset the errors associated with variance losses.

5. Discussion

Comparisons between CCA and RegEM-Ridge show that the methods produce very similar results, with the exception of the larger variance losses observed in the RegEM-Ridge reconstructions. The source of variance losses is likely associated with the manner in which the eigenvalue spectra are truncated in the two methods. Ridge regression filters the eigenvalue spectrum using a continuous filter function; that is, there is no abrupt eigenvalue truncation like that used in CCA where modes that cannot be reliably calibrated are simply set to zero. This was indeed one reason why RegEM-Ridge was

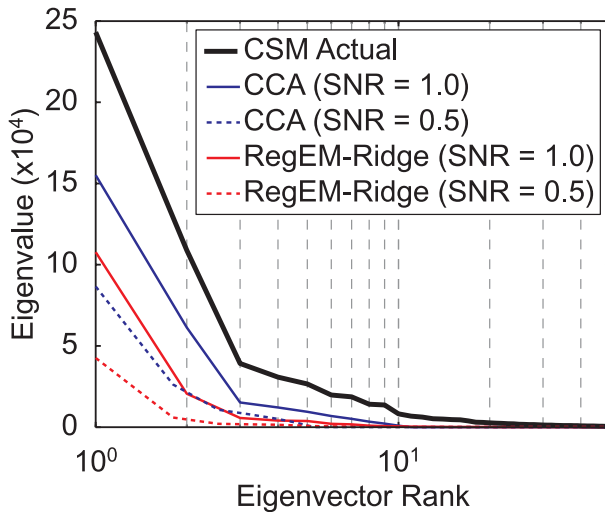


FIG. 11. Eigenspectra computed from the true model temperature field and the CCA and RegEM-Ridge reconstructed temperature fields during the reconstructed interval (850–1855 C.E.). The CCA spectra have the characteristic truncation to zero at the selected rank, whereas the RegEM-Ridge spectra reflect the continuous filtration constraint applied in ridge regression.

originally proposed as a potentially advantageous method in CFR contexts (Schneider 2001). A consequence of the continuous filtering function, however, is the fact that leading modes may be overly dampened if only a small number of them carry a large percentage of the total variance, as in the case of the CFR application presently considered [cf. discussion surrounding Eq. (19) in Schneider (2001)]. By contrast, the finite truncation of the CCA method yields leading modes that are unaffected by the truncation. To demonstrate this fact, Fig. 11 plots the eigenspectra for the true model field and for the RegEM-Ridge and CCA CFRs at SNR levels of 1.0 and 0.5. The magnitudes of the RegEM-Ridge eigenvalues are strikingly reduced in comparison to those of CCA. Apart from their scaling, however, Fig. 9 and the similarity of the correlation statistics for both methods shown in Figs. 7 and 10 indicate that the two methods are reconstructing similar patterns, and differ primarily by the dampened variability of the leading modes in the RegEM-Ridge spectrum. Regarding the smaller differences between the CCA and RegEM-Ridge reconstructions, there are additional methodological choices that are likely contributors, for example, differences in the cross-validation and parameter choices that the two methods employ. Exploring further differences between the CCA and RegEM-Ridge methods would be insightful for understanding the small differences in the reconstructions that they generate and should be the subject of further research. Nevertheless, the results provided herein indicate that the methods produce

broadly consistent reconstructions, except for the larger variance losses observed for RegEM-Ridge.

The above discussion is relevant to the important and yet to be explained difference between pseudoproxy CFRs derived using RegEM-Ridge and RegEM using truncated total least squares (RegEM-TTLS) (Mann et al. 2007a). This latter method has been shown to perform well in one pseudoproxy context (Mann et al. 2007a), particularly in terms of its ability to reproduce the NH mean index, whereas the former has not (Smerdon and Kaplan 2007). The original explanation for the differences between the performance of RegEM-Ridge and RegEM-TTLS was tied to the selection of the ridge parameter by means of GCV in RegEM-Ridge (Mann et al. 2007a,c). Because GCV was not used within RegEM-TTLS, Mann et al. (2007a,c) concluded that the problem was specific to RegEM-Ridge. Smerdon et al. (2008b), however, demonstrated that the mean biases and variance losses in RegEM-Ridge were not associated with the GCV selection of the ridge parameter, making the Mann et al. (2007a,c) explanation implausible. The similarity between the CCA and RegEM-Ridge results presented herein further indicate that mean biases and variance losses in currently employed CFR methods are not tied to a specific methodological choice. Moreover, the similar shortcomings observed for the Mann et al. (1998) CFR method noted by von Storch et al. (2004, 2006) support the idea that the effects cannot be connected to something specific in RegEM-Ridge. It is therefore unlikely that differences in the reported performance of multiple CFRs can be specifically associated with the method of eigenvalue truncation or filtration, pointing to the need for an improved understanding of why the differences exist.

It is also important to highlight the observed concentration of the highest field correlations (and preserved variance) in areas with high pseudoproxy concentrations, a feature of both the CCA and RegEM-Ridge CFRs. Although this result may seem intuitive, it is not necessarily an expected characteristic of either the CCA or RegEM-Ridge methods. Both of these techniques attempt to reconstruct large-scale climate patterns by discarding smaller-scale modes of variability and noise. Despite this emphasis on large-scale patterns, the observed correlation distributions demonstrate that the methods perform best where dense sampling exists. This suggests that addition of low-noise proxy data outside of existing highly sampled regions should be an important priority for improvement of regional-scale CFR skill.

Given the above observation, it is important to better understand the origin of the observed skill concentrations and their dependence on the underlying character of the target field. In the case of the reported pseudoproxy experiments, the skill patterns are dependent on the

internal statistics of the model-simulated climate. Previous experiments have indicated that methodological performance is not strongly dependent on the employed model simulation. Integrations from two different GCMs were used by von Storch et al. (2004, 2006) to test the Mann et al. (1998) method, and results were consistent across the simulations in terms of the NH means. The authors also reported no significant dependence on the sampling distribution. Similarly, Mann et al. (2007a) indicated no significant sensitivity to the two GCM integrations or sampling distribution used to test RegEM-TTLS. Christiansen et al. (2009) used yet another model integration and method for generating ensemble statistics and observed mean biases and variance losses in NH means derived from multiple methods. It is therefore unlikely that differences in model integrations will affect the gross performance of reconstruction methods already reported. Nevertheless, the underlying field performance of CFRs is likely more sensitive to the spatial statistics of the model simulations and should be tested on multiple model integrations. More experiments using observational data (e.g., Evans et al. 2001, 2002) are also needed to determine whether the skill patterns of pseudoproxy experiments are similar to those estimated from real-world datasets.

The use of pseudoproxy experiments as a research tool has proceeded under the assumption that modeled climates and pseudoproxies approximate well the conditions in real-world reconstruction problems. This assumption may require the most caution, however, when interpreting results dependent on the underlying spatial statistics of the field and the associated teleconnections. Furthermore, noise structures in real-world proxies are undoubtedly more complicated than the white noise models used in this study. While it is appropriate to approach the results contained herein as a best-case scenario, further work is necessary to more faithfully capture the nonlinear, multivariate, and nonstationary noise characteristics that are likely present in many proxy series (e.g., North et al. 2006). For instance, tree-ring models have been developed to simulate dendroclimatic series with notable success (Evans et al. 2006; Anchukaitis et al. 2006) and can be used to simulate synthetic tree-ring chronologies for use in pseudoproxy studies. The seasonal dependencies of proxy records should also be considered in future work. Significant variations in field skill have been observed for multiproxy networks that target individual seasons (e.g., Pauling et al. 2003) and suggest that the annual pseudoproxy records used in most studies to date is another important idealization. Incorporating these more complicated proxy characteristics in pseudoproxy studies will provide more realistic evaluations of CFR methods. Recent work also has shown the importance of evaluating

ensembles of reconstructions generated from multiple noise realizations in both the proxy and target datasets (Christiansen et al. 2009). Not all differences between methods tested on individual noise realizations may be statistically significant when uncertainties due to random errors are incorporated. Christiansen et al. (2009) have shown this is the case for NH mean estimates, but such ensemble work has not been done in the context of reconstruction performance in the field. Future work to evaluate field skill in ensembles of CFRs is therefore highly warranted.

6. Conclusions

Successful application of the CCA method to the problem of reconstructing NH temperature fields during the last millennium has been demonstrated and evaluated using pseudoproxies. An element of this application involved the development of a selection procedure for the three CCA dimensions. We have demonstrated a “leave half out” cross-validation procedure that selects robust and parsimonious dimensional combinations while guarding against artificial skill in the reconstruction. Our experiments demonstrate that the CCA method faithfully reconstructs between 3 and 13 climatic patterns given a proxy distribution approximating the Mann et al. (1998) proxy network and a range of observational uncertainties from no noise to an SNR of 0.25. (The exact number of resolved patterns will of course vary with different noise realizations at a given SNR value and is idealized in the pseudoproxy framework.) Subsequent application of the CCA method to real-world climate proxies is thus easily attainable in future work. The transparency of the CCA method and its well-developed theoretical basis in the literature is a strong motivation for its application. These characteristics provide straightforward evaluations of the CCA model selection and the source of skill in derived reconstructions. The results of our pseudoproxy experiments, however, suggest that CFRs derived using CCA, just like those derived from RegEM-Ridge, should be interpreted carefully when applied to the problem of reconstructing large-scale climate patterns during the last several millennia.

Field correlations were shown to diminish significantly with increasing noise, particularly in regions with few or no pseudoproxies. Given that SNRs in real proxy records are estimated to be on the order of 0.4 (e.g., Mann et al. 2007a) and typically characterized by more complicated autoregressive and moving average structures than the white-noise models adopted herein, the observed skill reductions should be considered a best-case scenario. In real-world CFRs derived with CCA, the spatial patterns of field errors will depend on at least five factors: 1) the

spatial distribution of the proxies; 2) the magnitude and character of noise in the proxy network; 3) the spatial coherence of the target field, that is, the strength and character of its teleconnections; 4) the true historical variability of the climate during the reconstruction interval; and 5) the length of the calibration period used for estimating proxy-climate correlations. The dependence of the spatial skill associated with the CCA method to these factors requires further testing. Evaluation of the method using additional millennial simulations from GCMs or observational fields should be pursued to determine the robustness of the spatial skill dependencies that we have identified. More realistic pseudoproxy networks should also be considered that incorporate seasonal dependencies, multivariate climate responses, and autoregressive noise structures. The impact of these more complicated pseudoproxy characteristics should be considered specifically with regard to the field characteristics as we have outlined in the present manuscript, as opposed to the more widely evaluated performance of the NH mean. Their impact within different calibration scenarios is also important, particularly with regard to the length of the calibration interval and the range of climate variability represented in the calibration interval relative to the reconstruction interval (e.g., Jones et al. 2009).

Comparisons between reconstructions derived from CCA and RegEM-Ridge demonstrate strong similarities between the two methods, both in terms of the derived mean NH temperatures and the spatial characteristics of the reconstructed fields. These similarities are encouraging regarding the consistency of the two methods, but are also an indication that there may be problems endemic to the present generation of CFR methods used to reconstruct large-scale temperature patterns during the last millennium. Therefore, more research is needed to characterize the performance of multiple CFR methods in terms of their field performance and to draw distinct conclusions about the similarities and differences. These studies are particularly needed in the context of CFRs derived from real-world proxies as a means of deriving a better description of the uncertainties in present estimates of late-Holocene temperature variability.

The similarity between the CCA and RegEM-Ridge results further points to the need to understand the differences in the performance of the RegEM-Ridge and RegEM-TTLS methods. Resolving the origin of these differences is not only important for studies that have attempted to reconstruct temperatures over the last millennium (Rutherford et al. 2005; Mann et al. 2005, 2007a, 2008, 2009) but also for efforts that have applied RegEM in other contexts (e.g., Zhang et al. 2004; Steig et al. 2009). This necessity is further supported by the fact that

pseudoproxy experiments have demonstrated differences between the performance of the two RegEM approaches, while real-world reconstructions of late-Holocene temperatures derived from the two methods have not been notably different—at least in their representation of the NH mean (Mann et al. 2007a). Each of these observations indicates that the focus within the literature on only NH means is insufficient for evaluating CFR methods and their derived results. Explaining the performance differences between various CFR methods remains an open research question, but the persistence of similar problems in now multiple linear reconstruction methods suggests that caution must be exercised in the interpretation of published real-world CFR results.

Acknowledgments. Codes and data for the reconstructions performed in this paper are available online at http://www.ldeo.columbia.edu/~jsmerdon/2010_jclim_cca_supplement.html. We gratefully acknowledge three anonymous reviewers for their constructive criticism and useful suggestions, all of which helped to improve the manuscript. This research was supported by the National Science Foundation Grants ATM04-07909, ATM-0902436, and ATM-0902715 and by the National Oceanic and Atmospheric Administration, U.S. Department of Commerce, by Grant NA07OAR4310060 and NAOAR4320912, the latter under the Cooperative Institute for Climate Applications Research (CICAR). Part of this research was completed while DC was supported by a research internship from the Hughes Science Pipeline Project and JES was supported by a Mellon Postdoctoral Fellowship, both through the Department of Environmental Science at Barnard College. The statements, findings, conclusions, and recommendations are those of the authors and do not necessarily reflect the views of any of these organizations or agencies.

APPENDIX

Application of CCA to the Climate Field Reconstruction Problem

Beginning with the SVDs of the proxy and temperature matrices written in section 3b, we use multivariate linear regression with a matrix \mathbf{B}'

$$\mathbf{V}_t^{rT} = \mathbf{B}'\mathbf{V}_p^{rT} + \varepsilon_v$$

(ε_v is the residual error) to predict the prewhitened PCs of temperature using the prewhitened proxy PCs:

$$\hat{\mathbf{V}}_t^{rT} = \mathbf{B}'\mathbf{V}_p^{rT}.$$

Because the prewhitened PCs are orthonormal, $\mathbf{V}_p^{rT}\mathbf{V}_p^r = \mathbf{I}$ (i.e., the identity matrix), the expression for \mathbf{B}' simplifies to

$$\mathbf{B}' = (\mathbf{V}_t^r \mathbf{V}_p^r) (\mathbf{V}_p^{rT} \mathbf{V}_p^r)^{-1} = \mathbf{V}_t^r \mathbf{V}_p^r.$$

The last expression for \mathbf{B}' can be decomposed using SVD,

$$\mathbf{B}' = \mathbf{V}_t^r \mathbf{V}_p^r = \mathbf{O}_t^r \boldsymbol{\Sigma}_{\text{cca}}^r \mathbf{O}_p^{rT}, \quad (\text{A1})$$

and can then be truncated by retaining only $d_{\text{cca}} \leq \min(d_p, d_t)$ leading singular values and corresponding patterns:

$$\mathbf{B}' = \mathbf{O}_t^r \boldsymbol{\Sigma}_{\text{cca}}^r \mathbf{O}_p^{rT}. \quad (\text{A2})$$

Prediction of the prewhitened temperature PCs using \mathbf{B}' instead of \mathbf{B} , that is,

$$\hat{\mathbf{V}}_t^{rT} = \mathbf{O}_t^r \boldsymbol{\Sigma}_{\text{cca}}^r \mathbf{O}_p^{rT} \mathbf{V}_p^{rT},$$

transforms into a simple form

$$\hat{\mathbf{Q}}_t^T = \boldsymbol{\Sigma}_{\text{cca}}^r \mathbf{O}_p^T \quad (\text{A3})$$

if written in terms of the CCA time series; these are projections of the vectors \mathbf{V}_t^r and \mathbf{V}_p^r onto the sets of patterns \mathbf{O}_t^r and \mathbf{O}_p^r respectively:

$$\mathbf{Q}_t = \mathbf{V}_t^r \mathbf{O}_t^r, \quad \mathbf{Q}_p = \mathbf{V}_p^r \mathbf{O}_p^r. \quad (\text{A4})$$

Similarly, the predicted $\hat{\mathbf{Q}}_t$ corresponds to the predicted prewhitened temperature PCs $\hat{\mathbf{V}}_t^r$:

$$\hat{\mathbf{Q}}_t = \hat{\mathbf{V}}_t^r \mathbf{O}_t^r.$$

To obtain the CCA time series, \mathbf{Q}_t , and \mathbf{Q}_p , directly from the standardized datasets, it is convenient to define the weight matrices,

$$\mathbf{W}_t = \mathbf{U}_t^r (\boldsymbol{\Sigma}_t^r)^{-1} \mathbf{O}_t^r, \quad \mathbf{W}_p = \mathbf{U}_p^r (\boldsymbol{\Sigma}_p^r)^{-1} \mathbf{O}_p^r, \quad (\text{A5})$$

so that

$$\mathbf{Q}_t^T = \mathbf{W}_t^T \mathbf{T}', \quad \mathbf{Q}_p^T = \mathbf{W}_p^T \mathbf{P}', \quad (\text{A6})$$

where Eqs. (5) and (6) and the orthonormality of the truncated EOF sets of \mathbf{U}_t^r and \mathbf{U}_p^r that is, columns, were used.

It follows from (A4) that the columns of \mathbf{Q}_t and \mathbf{Q}_p are orthonormal sets. Moreover, inserting (A4) into (A1) yields

$$\mathbf{Q}_t^T \mathbf{Q}_p = \boldsymbol{\Sigma}_{\text{cca}}^r.$$

Hence, the columns of \mathbf{Q}_t and \mathbf{Q}_p with different ordering are orthogonal, while those with the same ordering are

positively correlated. The correlation coefficients of these latter columns are equal to the diagonal elements of $\boldsymbol{\Sigma}_{\text{cca}}^r$ and are called canonical correlations. Because of the SVD decomposition in (A1), these are maximized in the following sense: the correlation coefficient between the first columns of \mathbf{Q}_t and \mathbf{Q}_p is the largest among the projections of \mathbf{V}_t^r and \mathbf{V}_p^r on any unit length vectors (patterns); these maximizing patterns are the first columns of \mathbf{O}_t^r and \mathbf{O}_p^r , respectively. The remaining correlation coefficients are arranged in descending order, that is, the coefficient between the second columns of \mathbf{Q}_t and \mathbf{Q}_p is the largest among projections of \mathbf{V}_t^r and \mathbf{V}_p^r on unit length vectors orthogonal to the first columns of \mathbf{O}_t^r and \mathbf{O}_p^r , respectively, and the patterns that achieve the latter correlation are the second columns of \mathbf{O}_t^r and \mathbf{O}_p^r . The correlation coefficient between the third columns of \mathbf{Q}_t and \mathbf{Q}_p is the largest among projections of \mathbf{V}_t^r and \mathbf{V}_p^r on unit length vectors orthogonal to the first and second columns of \mathbf{O}_t^r and \mathbf{O}_p^r , and so on.

The predictions of the CCA temperature time series by (A3) amount to a simple multiplication of the CCA time series of the proxies by the diagonal elements of $\boldsymbol{\Sigma}_{\text{cca}}^r$. To perform these predictions for the fields of temperature on the basis of the original proxy data, however, we require the spatial patterns of their regression on the CCA time series:

$$\mathbf{T}' = \mathbf{C}_t \mathbf{Q}_t^T + \boldsymbol{\varepsilon}_t, \quad \mathbf{P}' = \mathbf{C}_p \mathbf{Q}_p^T + \boldsymbol{\varepsilon}_p.$$

To determine \mathbf{C}_p and \mathbf{C}_t (the CCA patterns), or the CCA homogeneous covariance maps, we use the orthonormality of the CCA time series and the decomposition in (4):

$$\begin{aligned} \mathbf{C}_p &= (\mathbf{P}' \mathbf{Q}_p) (\mathbf{Q}_p^T \mathbf{Q}_p)^{-1} = \mathbf{P}' \mathbf{Q}_p \\ &= \mathbf{U}_p^r \boldsymbol{\Sigma}_p^r \mathbf{V}_p^{rT} \mathbf{V}_p^r \mathbf{O}_p^r = \mathbf{U}_p^r \boldsymbol{\Sigma}_p^r \mathbf{O}_p^r, \end{aligned} \quad (\text{A7})$$

and similarly

$$\mathbf{C}_t = \mathbf{T}' \mathbf{Q}_t = \mathbf{U}_t^r \boldsymbol{\Sigma}_t^r \mathbf{O}_t^r. \quad (\text{A8})$$

Thus, the use of the low-rank CCA approximations in (5), (6), and (A2) in the regression matrix formula given in (2) results in

$$\begin{aligned} \mathbf{B}_{\text{cca}} &= \mathbf{U}_t^r \boldsymbol{\Sigma}_t^r \mathbf{V}_t^{rT} \mathbf{V}_p^r (\boldsymbol{\Sigma}_p^r)^{-1} \mathbf{U}_p^{rT} \\ &= \mathbf{U}_t^r \boldsymbol{\Sigma}_t^r \mathbf{O}_t^r \boldsymbol{\Sigma}_{\text{cca}}^r \mathbf{O}_p^{rT} (\boldsymbol{\Sigma}_p^r)^{-1} \mathbf{U}_p^{rT}, \end{aligned}$$

if the inverse of the proxy covariance matrix is replaced by the pseudoinverse (Golub and Van Loan 1996):

$$(\mathbf{P}' \mathbf{P}'^T)^{-1} \rightarrow (\mathbf{P}' \mathbf{P}'^T)^+ = (\mathbf{P}' \mathbf{P}'^T)^+ = \mathbf{U}_p^r (\boldsymbol{\Sigma}_p^r)^{-2} \mathbf{U}_p^{rT}.$$

Given the definitions in Eqs. (A5) and (A8), \mathbf{B}_{cca} takes a simple form:

$$\mathbf{B}_{\text{cca}} = \mathbf{C}_t \Sigma_{\text{cca}}^r \mathbf{W}_p^T \quad (\text{A9})$$

REFERENCES

- Ammann, C., and E. Wahl, 2007: The importance of the geophysical context in statistical evaluations of climate reconstruction procedures. *Climatic Change*, **85**, 71–88.
- , F. Joos, D. S. Schimel, B. L. Otto-Bliesner, and R. A. Tomas, 2007: Solar influence on climate during the past millennium: Results from transient simulations with the NCAR Climate System Model. *Proc. Natl. Acad. Sci. USA*, **104**, 3713–3718.
- Anchukaitis, K. J., M. N. Evans, A. Kaplan, E. A. Vaganov, M. K. Hughes, H. D. Grissino-Mayer, and M. A. Cane, 2006: Forward modeling of regional scale tree-ring patterns in the southeastern United States and the recent influence of summer drought. *Geophys. Res. Lett.*, **33**, L04705, doi:10.1029/2005GL025050.
- Anderson, T. W., 1984: *An Introduction to Multivariate Statistical Analysis*. 2nd ed. Wiley-Interscience, 704 pp.
- Barnett, T., and R. Preisendorfer, 1987: Origins and levels of monthly and seasonal forecast skill for United States surface air temperature determined by canonical correlation analysis. *Mon. Wea. Rev.*, **115**, 1825–1850.
- Beltrami, H., 2002: Climate from borehole data: Energy fluxes and temperatures since 1500. *Geophys. Res. Lett.*, **29**, 2111, doi:10.1029/2002GL015702.
- Bradley, R. S., M. K. Hughes, and H. F. Diaz, 2003: Climate in medieval time. *Science*, **302**, 404–405.
- Bretherton, C., C. Smith, and J. M. Wallace, 1992: An intercomparison of methods for finding coupled patterns in climate data. *J. Climate*, **5**, 541–560.
- Briffa, K. R., 2000: Annual climate variability in the Holocene: Interpreting the message of ancient trees. *Quat. Sci. Rev.*, **19**, 87–105.
- , and T. J. Osborn, 2002: Blowing hot and cold. *Science*, **295**, 2227–2228.
- , —, F. H. Schweingruber, I. C. Harris, P. D. Jones, S. G. Shiyatov, and E. A. Vaganov, 2001: Low-frequency temperature variations from a northern tree ring density network. *J. Geophys. Res.*, **106**, 2929–2941.
- Broecker, W. S., 2001: Paleoclimate: Was the medieval warm period global? *Science*, **291**, 1497–1499.
- Bürger, G., and U. Cubasch, 2005: Are multiproxy climate reconstructions robust? *Geophys. Res. Lett.*, **32**, L23711, doi:10.1029/2005GL024155.
- , I. Fast, and U. Cubasch, 2006: Climate reconstruction by regression. *Tellus*, **58A**, 227–235.
- Casty, C., D. Handorf, and M. Sempf, 2005: Combined winter climate regimes over the North Atlantic/European sector 1766–2000. *Geophys. Res. Lett.*, **32**, L13801, doi:10.1029/2005GL022431.
- Cherry, S., 1996: Singular value decomposition analysis and canonical correlation analysis. *J. Climate*, **9**, 2003–2009.
- Christiansen, B., T. Schmith, and P. Thejll, 2009: A surrogate ensemble study of climate reconstruction methods: Stochasticity and robustness. *J. Climate*, **22**, 951–976.
- , —, and —, 2010: Reply. *J. Climate*, **23**, 2839–2844.
- Cook, E. R., K. R. Briffa, and P. D. Jones, 1994: Spatial regression methods in dendroclimatology: A review and comparison of two techniques. *Int. J. Climatol.*, **14**, 379–402.
- , J. Esper, and R. D'Arrigo, 2004: Extra-tropical Northern Hemisphere land temperature variability over the past 1000 years. *Quat. Sci. Rev.*, **23**, 2063–2074.
- Crowley, T. J., and T. S. Lowery, 2000: How warm was the medieval warm period? *Ambio*, **29**, 51–54.
- D'Arrigo, R., R. Wilson, and G. Jacoby, 2006: On the long-term context for late twentieth century warming. *J. Geophys. Res.*, **111**, D03103, doi:10.1029/2005JD006352.
- , —, and A. Tudhope, 2009: The impact of volcanic forcing on tropical temperatures during the past four centuries. *Nat. Geosci.*, **2**, 51–56.
- Esper, J., E. R. Cook, and F. H. Schweingruber, 2002: Low-frequency signals in long tree-ring chronologies for reconstructing past temperature variability. *Science*, **295**, 2250–2253.
- , D. C. Frank, R. J. S. Wilson, and K. R. Briffa, 2005: Effect of scaling and regression on reconstructed temperature amplitude for the past millennium. *Geophys. Res. Lett.*, **32**, L07711, doi:10.1029/2004GL021236.
- Evans, M. N., A. Kaplan, M. A. Cane, and R. Villalba, 2001: Globality and optimality in climate field reconstructions from proxy data. *Present and Past Inter-Hemispheric Linkages in the Americas and Their Societal Effects*, V. Markgraf, Ed., Cambridge University Press, 53–72.
- , —, and —, 2002: Pacific sea surface temperature field reconstruction from coral $\delta^{18}\text{O}$ data using reduced space objective analysis. *Paleoceanography*, **17**, 1007, doi:10.1029/2000PA000590.
- , B. K. Reichert, A. Kaplan, K. J. Anchukaitis, E. A. Vaganov, M. K. Hughes, and M. A. Cane, 2006: A forward modeling approach to paleoclimatic interpretation of tree-ring data. *J. Geophys. Res.*, **111**, G03008, doi:10.1029/2006JG000166.
- Folland, C. K., and Coauthors, 2001: Observed climate variability and change. *Climate Change 2001: The Scientific Basis*, J. T. Houghton et al., Eds., Cambridge University Press, 99–181.
- Fritts, H. C., T. J. Blasing, B. P. Hayden, and J. E. Kutzbach, 1971: Multivariate techniques for specifying tree-growth and climate relationships and for reconstructing anomalies in paleoclimate. *J. Appl. Meteor.*, **10**, 845–864.
- Golub, G. H., and C. F. Van Loan, 1996: *Matrix Computations*. 3rd ed. The Johns Hopkins University Press, 694 pp.
- González-Rouco, F., H. von Storch, and E. Zorita, 2003: Deep soil temperature as proxy for surface air-temperature in a coupled model simulation of the last thousand years. *Geophys. Res. Lett.*, **30**, 2116, doi:10.1029/2003GL018264.
- González-Rouco, J. F., H. Beltrami, E. Zorita, and H. von Storch, 2006: Simulation and inversion of borehole temperature profiles in surrogate climates: Spatial distribution and surface coupling. *Geophys. Res. Lett.*, **33**, L01703, doi:10.1029/2005GL024693.
- Groverman, B. S., and H. E. Landsberg, 1979: Simulated Northern Hemisphere temperature departures 1579–1880. *Geophys. Res. Lett.*, **6**, 767–770.
- Harris, R. N., and D. S. Chapman, 2001: Mid-latitude (30°N–60°N) climatic warming inferred by combining borehole temperatures with surface air temperatures. *Geophys. Res. Lett.*, **28**, 747–750.
- Hegerl, G. C., T. Crowley, M. Allen, W. T. Hyde, H. Pollack, J. Smerdon, and E. Zorita, 2007: Detection of human influence on a new 1500-yr climate reconstruction. *J. Climate*, **20**, 650–666.
- Huang, S., H. N. Pollack, and P. Y. Shen, 2000: Temperature trends over the last five centuries reconstructed from borehole temperatures. *Nature*, **403**, 756–758.

- Hughes, M. K., and H. F. Diaz, 1994: Was there a medieval warm period, and if so, where and when? *Climatic Change*, **26**, 109–142.
- Huybers, P., 2005: Comment on “Hockey Sticks, Principal Components, and Spurious Significance” by S. McIntyre and R. McKittrick. *Geophys. Res. Lett.*, **32**, L20705, doi:10.1029/2005GL023395.
- Jansen, E., and Coauthors, 2007: Palaeoclimate. *Climate Change 2007: The Physical Science Basis*, S. Solomon et al., Eds., Cambridge University Press, 433–497.
- Jones, P. D., and M. E. Mann, 2004: Climate over past millennia. *Rev. Geophys.*, **42**, RG2002, doi:10.1029/2003RG000143.
- , K. R. Briffa, T. P. Barnett, and S. F. B. Tett, 1998: High-resolution palaeoclimatic records for the last millennium: Interpretation, integration and comparison with general circulation model control-run temperatures. *Holocene*, **8**, 455–471.
- , M. New, D. E. Parker, S. Martin, and J. G. Rigor, 1999: Surface air temperature and its changes over the past 150 years. *Rev. Geophys.*, **37**, 173–199.
- , and Coauthors, 2009: High-resolution paleoclimatology of the last millennium: A review of current status and future prospects. *Holocene*, **19**, 3–49.
- Küttel, M., J. Luterbacher, E. Zorita, E. Xoplaki, N. Riedwyl, and H. Wanner, 2007: Testing a European winter surface temperature reconstruction in a surrogate climate. *Geophys. Res. Lett.*, **34**, L07710, doi:10.1029/2006GL027907.
- Lee, T. C. K., F. W. Zwiers, and M. Tsao, 2007: Evaluation of proxy-based millennial reconstruction methods. *Climate Dyn.*, **31**, 263–281.
- Luterbacher, J., C. Schmutz, D. Gyalistras, E. Xoplaki, and H. Wanner, 1999: Reconstruction of monthly NAO and EU indices back to AD 1675. *Geophys. Res. Lett.*, **26**, 2745–2748.
- , and Coauthors, 2000: Reconstruction of monthly mean sea level pressure over Europe for the late Maunder Minimum period (1675–1715). *Int. J. Climatol.*, **20**, 1049–1066.
- , D. Dietrich, E. Xoplaki, M. Grosjean, and H. Wanner, 2004: European seasonal and annual temperature variability, trends, and extremes since 1500. *Science*, **303**, 1499–1503.
- Mann, M. E., 2002: The value of multiple proxies. *Science*, **297**, 1481–1482.
- , and S. Rutherford, 2002: Climate reconstruction using ‘pseudoproxies.’ *Geophys. Res. Lett.*, **29**, 1501, doi:10.1029/2001GL014554.
- , R. S. Bradley, and M. K. Hughes, 1998: Global-scale temperature patterns and climate forcing over the past six centuries. *Nature*, **392**, 779–787.
- , —, and —, 1999: Northern Hemisphere temperatures during the past millennium: Inferences, uncertainties, and limitations. *Geophys. Res. Lett.*, **26**, 759–762.
- , and Coauthors, 2003: On past temperatures and anomalous late 20th-century warmth. *Eos, Trans. Amer. Geophys. Union*, **84**, 256–258.
- , S. Rutherford, E. Wahl, and C. Ammann, 2005: Testing the fidelity of methods used in proxy-based reconstructions of past climate. *J. Climate*, **18**, 4097–4107.
- , —, —, and —, 2007a: Robustness of proxy-based climate field reconstruction methods. *J. Geophys. Res.*, **112**, D12109, doi:10.1029/2006JD008272.
- , —, —, and —, 2007b: Reply. *J. Climate*, **20**, 3699–3703.
- , —, —, and —, 2007c: Reply. *J. Climate*, **20**, 5671–5674.
- , Z. Zhang, M. K. Hughes, R. S. Bradley, S. K. Miller, S. Rutherford, and F. Ni, 2008: Proxy-based reconstructions of hemispheric and global surface temperature variations over the past two millennia. *Proc. Natl. Acad. Sci. USA*, **105**, 13 252–13 257.
- , and Coauthors, 2009: Global signatures and dynamical origins of the little ice age and the medieval climate anomaly. *Science*, **326**, 1256–1260.
- McIntyre, S., and R. McKittrick, 2005: Hockey sticks, principal components, and spurious significance. *Geophys. Res. Lett.*, **32**, L03710, doi:10.1029/2004GL021750.
- Moberg, A., D. M. Sonechkin, K. Holmgren, N. M. Datsenko, and W. Karlen, 2005: Highly variable Northern Hemisphere temperature reconstructed from low- and high-resolution proxy data. *Nature*, **433**, 613–617.
- , R. Mohammad, and T. Mauritsen, 2008: Analysis of the Moberg et al. (2005) hemispheric temperature reconstruction. *Climate Dyn.*, **31**, 957–971.
- North, G. R., and Coauthors, 2006: *Surface Temperature Reconstructions for the Last 2000 Years*. National Academies Press, 196 pp.
- Pauling, A., J. Luterbacher, and H. Wanner, 2003: Evaluation of proxies for European and North Atlantic temperature field reconstructions. *Geophys. Res. Lett.*, **30**, 1787, doi:10.1029/2003GL017589.
- , —, C. Casty, and H. Wanner, 2006: Five hundred years of gridded high-resolution precipitation reconstructions over Europe and the connection to large-scale circulation. *Climate Dyn.*, **26**, 387–405.
- Pollack, H. N., and J. E. Smerdon, 2004: Borehole climate reconstructions: Spatial structure and hemispheric averages. *J. Geophys. Res.*, **109**, D11106, doi:10.1029/2003JD004163.
- Preisendorfer, R., F. Zwiers, and T. P. Barnett, 1981: *Foundations of Principal Component Selection Rules*. SIO Reference Series, No. 81-4, Scripps Institution of Oceanography, 192 pp.
- Riedwyl, N., M. Küttel, J. Luterbacher, and H. Wanner, 2009: Comparison of climate field reconstruction techniques: Application to Europe. *Climate Dyn.*, **32**, 381–395.
- Rutherford, S., and M. E. Mann, 2004: Correction to “Optimal surface temperature reconstructions using terrestrial borehole data.” *J. Geophys. Res.*, **109**, D11107, doi:10.1029/2003JD004290.
- , —, T. J. Osborn, R. S. Bradley, K. R. Briffa, M. K. Hughes, and P. D. Jones, 2005: Proxy-based Northern Hemisphere surface temperature reconstructions: Sensitivity to methodology, predictor network, target season, and target domain. *J. Climate*, **18**, 2308–2329.
- , —, E. Wahl, and C. Ammann, 2008: Reply to comment by Jason E. Smerdon et al. on “Robustness of Proxy-Based Climate Field Reconstruction Methods.” *J. Geophys. Res.*, **113**, D18107, doi:10.1029/2008JD009964.
- , —, C. M. Ammann, and E. R. Wahl, 2010: Comments on “A surrogate ensemble study of climate reconstruction methods: Stochasticity and robustness.” *J. Climate*, **23**, 2832–2838.
- Schneider, T., 2001: Analysis of incomplete climate data: Estimation of mean values and covariance matrices and imputation of missing values. *J. Climate*, **14**, 853–887.
- Smerdon, J. E., and A. Kaplan, 2007: Comments on “Testing the fidelity of methods used in proxy-based reconstructions of past climate”: The role of the standardization interval. *J. Climate*, **20**, 5666–5670.
- , J. F. González-Rouco, and E. Zorita, 2008a: Comment on “Robustness of Proxy-Based Climate Field Reconstruction Methods” by Michael E. Mann et al. *J. Geophys. Res.*, **113**, D18106, doi:10.1029/2007JD009542.

- , A. Kaplan, and D. Chang, 2008b: On the standardization sensitivity of RegEM climate field reconstructions. *J. Climate*, **21**, 6710–6723.
- , —, and D. E. Amrhein, 2010: Erroneous model field representations in multiple pseudoproxy studies: Corrections and Implications. *J. Climate*, **23**, 5548–5554.
- Steig, E. J., D. P. Schneider, S. D. Rutherford, M. E. Mann, J. C. Comiso, and D. T. Shindell, 2009: Warming of the Antarctic ice sheet surface since the 1957 International Geophysical Year. *Nature*, **457**, 459–463.
- Tingley, M. P., and P. Huybers, 2010a: A Bayesian algorithm for reconstructing climate anomalies in space and time. Part I: Development and applications to paleoclimate reconstruction problems. *J. Climate*, **23**, 2759–2781.
- , and —, 2010b: A Bayesian algorithm for reconstructing climate anomalies in space and time. Part II: Comparison with the regularized expectation–maximization algorithm. *J. Climate*, **23**, 2782–2800.
- Tippett, M. K., M. Barlow, and B. Lyon, 2003: Statistical correction of central southwest Asia winter precipitation simulations. *Int. J. Climatol.*, **23**, 1421–1433.
- , T. DelSole, S. J. Mason, and A. G. Barnston, 2008: Regression-based methods for finding coupled patterns. *J. Climate*, **21**, 4384–4398.
- von Storch, H., and F. W. Zwiers, 1999: *Statistical Analysis in Climate Research*. Cambridge University Press, 494 pp.
- , and E. Zorita, 2005: Comment on “Hockey Sticks, Principal Components, and Spurious Significance” by S. McIntyre and R. McKittrick. *Geophys. Res. Lett.*, **32**, L20701, doi:10.1029/2005GL022753.
- , —, J. M. Jones, Y. Dimitriev, F. González-Rouco, and S. F. B. Tett, 2004: Reconstructing past climate from noisy data. *Science*, **306**, 679–682.
- , —, —, F. González-Rouco, and S. F. B. Tett, 2006: Response to comment on “Reconstructing Past Climate from Noisy Data.” *Science*, **312**, 529.
- Wahl, E. R., and C. M. Ammann, 2007: Robustness of the Mann, Bradley, Hughes reconstruction of surface temperatures: Examination of criticisms based on the nature and processing of proxy climate evidence. *Climatic Change*, **85**, 33–69.
- , D. M. Ritson, and C. M. Ammann, 2006: Comment on “Reconstructing Past Climate from Noisy Data.” *Science*, **312**, 529b.
- Wilks, D. S., 1995: *Statistical Methods in the Atmospheric Sciences*. Academic Press, 467 pp.
- Xoplaki, E., J. Luterbacher, H. Paeth, D. Dietrich, N. Steiner, M. Grosjean, and H. Wanner, 2005: European spring and autumn temperature variability and change of extremes over the last half millennium. *Geophys. Res. Lett.*, **32**, L15713, doi:10.1029/2005GL023424.
- Zhang, Z., M. E. Mann, and E. R. Cook, 2004: Alternative methods of proxy-based climate field reconstruction: Application to summer drought over the conterminous United States back to AD 1700 from tree-ring data. *Holocene*, **14**, 502–516.
- Zorita, E., F. González-Rouco, and H. von Storch, 2007: Comments on “Testing the fidelity of methods used in proxy-based reconstructions of past climate.” *J. Climate*, **20**, 3693–3698.